Journal of Fluids and Structures 23 (2007) 59–83

JOURNAL OF
FLUIDS AND
STRUCTURES

www.elsevier.com/locate/jfs

Hydrodynamic forces on dual cylinders of different diameters in steady currents

M. Zhao[a,*], L. Cheng[a], B. Teng[b], G. Dong[b]

[a]*School of Civil and Resource Engineering, The University of Western Australia, 35 Stirling Highway, Crawley, WA 6009, Australia*
[b]*State Key Laboratory of Coastal and Offshore Engineering, Dalian University of Technology, Dalian 116024, China*

Received 5 July 2005; accepted 14 July 2006

Abstract

Turbulent flow past two circular cylinders of different diameters is numerically investigated. The two-dimensional Reynolds-averaged Navier–Stokes equations are solved by using a finite element method with a k–ω turbulence closure. Following a relevant numerical model validation process, effects of cylinder gap-to-diameter ratio, the angular position of the smaller cylinder and the diameter ratio of cylinders on the vortex shedding and the forces on the cylinders are investigated using the numerical model. It is found that the relative position of the small cylinder has significant effects on the hydrodynamic force and vortex shedding characteristics of the cylinders.

1. Introduction

Flow around two cylinders of different diameters has close relevance to flow around a piggyback pipeline in offshore oil and gas explorations. A piggyback pipeline normally comprises of one (or more) small pipe (or pipes) and a large pipe. The diameter ratio of the small pipe to the large pipe is often in the range of 0.1–0.5. The small and the large pipes are often strapped together to form a pipeline bundle. Pipes in a bundle could either be in contact or separate, depending on design and installation requirements. Design of such pipeline bundles requires the evaluation of hydrodynamic forces acting on the bundle. Due to the lack of reliable hydrodynamic data on such pipeline bundles, it is often done to approximate a bundle of pipelines as a single pipeline of an equivalent diameter (equals to the sum of the two diameters and the gap between the two cylinders) in calculating the hydrodynamic forces. Such an approximation has not been adequately validated.

There has not been extensive research on flow around two cylinders of different diameters. Most of the reported studies on two-cylinder configurations were concerned with two cylinders of an identical diameter [e.g., Zdravkovich (1977, 1987), Bearman and Wadcock (1973), Williamson (1985), Meneghini et al. (2001)]. Strykowski and Sreenivasan (1990) investigated the suppression of vortex shedding from a circular cylinder by introducing a small circular cylinder at low Reynolds numbers. Sakamoto et al. (1991) and Sakamoto and Haniu (1994) studied the suppression of hydrodynamic forces acting on a square cylinder and a circular cylinder, respectively, in the sub-critical Reynolds number regime. Dalton et al. (2001) simulated the suppression of lift force on a circular cylinder by a small cylinder.

---

[*] Corresponding author. Tel.: +61 8 6488 7356; fax: +61 8 6488 1044.
E-mail address: zhao@civil.uwa.edu.au (M. Zhao).

doi:10.1016/j.jfluidstructs.2006.07.003

The diameter ratio of the small cylinder to the large cylinder in the above-mentioned studies was quite small in comparison with typical diameter ratios used in offshore industry for pipelines.

Recently, Zhao et al. (2005) carried out a numerical study of flow around two cylinders of different diameters at a relatively low Reynolds number (500 based on the diameter of the large cylinder). The effects of the small cylinder on the flow around and forces on the two cylinders were investigated for different gap ratios and position angles for a diameter ratio of 0.25. Since the study was carried out at a rather low Reynolds number, the application of the results by Zhao et al. (2005) to practical engineering problems (Reynolds number often ranging from 10^4 to 10^6) is not straightforward.

The aim of this study is to extend the study by Zhao et al. (2005) to a higher Reynolds number (5×10^4). The two-dimensional Reynolds-averaged Navier–Stokes equations are solved using a finite element method with a k–ω turbulence closure. The numerical model developed in this study is firstly validated against the experimental results reported in the literature (Tsutsui et al., 1997). Then, the effect of the position angle of the small cylinder on the hydrodynamic forces and vortex shedding frequency is studied for a diameter ratio of 0.5 between the small cylinder diameter (d) and the large cylinder diameter (D). The position angle of the small cylinder examined ranges from 0 to 180° and the gaps between the two cylinders (G) are $0.05D$, $0.1D$, $0.2D$ and $0.4D$. The effects of the diameter ratio on the shedding flow are also studied. Computations are carried out for d/D ranging from 0.1 to 1.0 at constant position angle of the small cylinder of 90°.

2. Governing equations

A typical two pipe piggyback pipeline configuration considered in this study is sketched in Fig. 1. The small cylinder represents the small pipeline and the large cylinder represents the large pipeline. The position of the small cylinder relative to the large one is uniquely defined by the gap between the two cylinders G and the angle α as shown in Fig. 1. In Fig. 1, a steady uniform flow approaches the cylinders from the negative direction of the x-axis, and θ is positive in the clockwise direction, starting from the front point of the cylinder.

The governing equations are the two-dimensional incompressible Reynolds-averaged Navier–Stokes equations and the continuity equation. The nondimensional equations in the Cartesian coordinate system can be written as

$$\frac{\partial u_i}{\partial t} + u_j \frac{\partial u_i}{\partial x_j} = -\frac{\partial}{\partial x_i}\left(p + \frac{2}{3}k\right) + \frac{\partial}{\partial x_j}\left(\frac{1}{\mathrm{Re}}\frac{\partial u_i}{\partial x_j} + 2\nu_t S_{ij}\right), \tag{1}$$

$$\frac{\partial u_i}{\partial x_i} = 0, \tag{2}$$

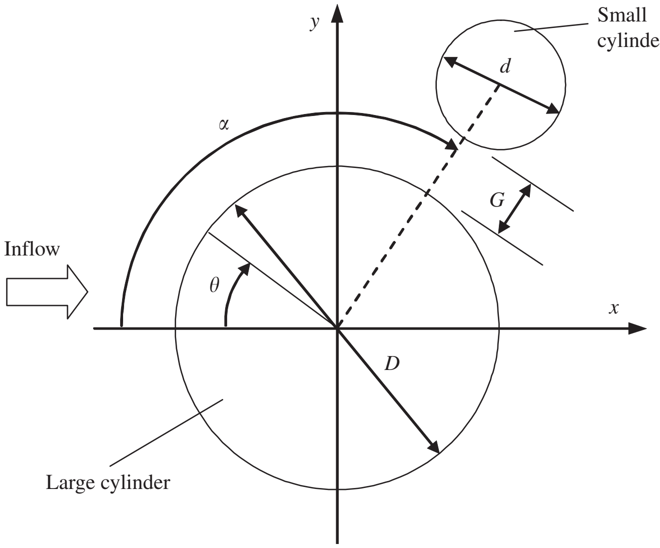

Fig. 1. Definition sketch.

Table 1
Model constants for the high Reynolds number k–ω model

σ^*	σ	β^*	β	γ	γ^*
0.5	0.5	0.09	0.075	0.553	1.0

where x_i ($i = 1$ and 2) is the Cartesian coordinate, u_i is the velocity component, p is the pressure, k is the turbulent kinetic energy, Re ($= UD/\nu$) is the Reynolds number defined by the free stream velocity U and the large cylinder diameter D; ν is the molecular kinetic viscosity, t is time, S_{ij} is the mean strain rate tensor which is defined as

$$S_{ij} = \frac{1}{2}\left(\frac{\partial u_i}{\partial x_j} + \frac{\partial u_j}{\partial x_i}\right). \tag{3}$$

The k–ω two-equation model (Wilcox, 1988, 1994) is used to determine the turbulent kinetic energy k and the turbulent viscosity ν_t in this study. The equations for k and ω are expressed as

$$\frac{\partial k}{\partial t} + u_j\frac{\partial k}{\partial x_j} = \frac{\partial}{\partial x_j}\left[\left(\frac{1}{\mathrm{Re}} + \sigma^*\nu_t\right)\frac{\partial k}{\partial x_j}\right] + P_k - \beta^*\omega k, \tag{4}$$

$$\frac{\partial \omega}{\partial t} + u_j\frac{\partial \omega}{\partial x_j} = \frac{\partial}{\partial x_j}\left[\left(\frac{1}{\mathrm{Re}} + \sigma\nu_t\right)\frac{\partial \omega}{\partial x_j}\right] + \frac{\gamma\omega}{k}P_k - \beta\omega^2, \tag{5}$$

where $\omega = \varepsilon/(\beta^* k)$ is the specific dissipation of turbulent kinetic energy, ε is the dissipation of turbulent kinetic energy, $P_k = 2\nu_t S_{ij}(\partial u_i/\partial x_j)$ is the turbulent kinetic energy production. The eddy viscosity ν_t in the k–ω model is calculated as

$$\nu_t = \gamma^*\frac{k}{\omega}. \tag{6}$$

The model closure coefficients in Eqs. (4)–(6) for high Reynolds number are listed in Table 1.

3. Numerical method

The governing equations are discretized by a Galerkin finite element method in space. It is known that the conventional Galerkin discretization is equivalent to the central-difference approximation in finite difference method. Numerical instabilities often occur in central-difference solutions of the convective-diffusive equations because central-difference discretization has negative artificial diffusion. In this study, a streamline upwind scheme is applied by introducing an artificial diffusion term to the momentum equations. It should be noted that the artificial diffusion actually acts as a 'balancing diffusion' that balances the negative diffusion of the Galerkin treatment (Kelly et al., 1980; Brooks and Hughes, 1982). This streamline upwind method had been successfully applied in solving incompressible flow problems (Selvam, 1997; Jester and Kallinderis, 2003). The diffusion term added in the momentum equations is as (Brooks and Hughes, 1982)

$$\tilde{k}\frac{\partial}{\partial x_k}\left(u'_j u'_k \frac{\partial u_i}{\partial x_j}\right), \tag{7}$$

where $u'_i = u_i/\|\boldsymbol{u}\|$ with $\|\boldsymbol{u}\|$ being the magnitude of the velocity defined as $\|\boldsymbol{u}\|^2 = u_i u_i$, the parameter $\tilde{k}$ is defined as (Brooks and Hughes, 1982; Jester and Kallinderis, 2003)

$$\tilde{k} = \tilde{\xi}\|u_e\|h_e/2, \tag{8}$$

$$\tilde{\xi} = \begin{cases} \mathrm{Re}_h/3, & \mathrm{Re}_h \leqslant 3, \\ 1, & \mathrm{Re}_h > 3, \end{cases} \tag{9}$$

in which $\|u_e\|$ is the magnitude of the velocity at the centroid of the element, h_e is the average edge length of the element, $\mathrm{Re}_h (= \|u_e\|h_e/\nu)$ is the cell Reynolds number. The streamline upwind scheme is also applied in the solution procedures for the k and ω equations.

A fractional step formulation is applied for the time integration of the momentum equation (Eq. (1)) (Meling and Dalherim, 1997; Meneghini et al., 2001). First, an intermediate velocity is computed by neglecting the pressure gradient terms. The pressure field is then calculated by solving the pressure Poisson equation. The final velocity is computed by including the pressure effect. In this study the streamline upwind scheme is applied in the computational procedure of the intermediate velocity. During a time increment from $t = n\Delta t$ to $(n+1)\Delta t$, with Δt being the computational time step, the algorithm of the time advancement scheme for the equations is as follows:

(i) Compute the intermediate velocity $\tilde{u}_i^{n+1}$ at time $t = (n+1)\Delta t$ by solving the momentum equations without pressure terms. The diffusion terms are considered implicitly and the convection terms are considered explicitly from the previous time step. The turbulent viscosity at the time level $n\Delta t$ is used in calculating the velocity components and the turbulent quantities. The parameter $\tilde{k}$ is also evaluated at the time level $n\Delta t$. The equation for computing $\tilde{u}_i^{n+1}$ is as follows:

$$\tilde{u}_i^{n+1} - \Delta t \frac{\partial}{\partial x_j}\left[\left(\frac{1}{\mathrm{Re}} + \nu_t^n\right)\left(\frac{\partial \tilde{u}_i^{n+1}}{\partial x_j} + \frac{\partial \tilde{u}_j^{n+1}}{\partial x_i}\right)\right] - \Delta t \tilde{k} \frac{\partial}{\partial x_k}\left(u_j^n u_k^n \frac{\partial \tilde{u}_i^{n+1}}{\partial x_j}\right) = u_i^n - \Delta t u_j^n \frac{\partial u_i^n}{\partial x_j}, \tag{10}$$

where the last term of the left-hand side of Eq. (10) is the artificial diffusive term.

(ii) The intermediate velocity field does not, in general, satisfy the continuity equation. The pressure at the time $t = (n+1)\Delta t$ is computed to enforce the continuity in the final velocity field. The pressure is computed by solving the following pressure Poisson equation (can be obtained by substituting Eq. (12) into the continuity Eq. (2)),

$$\frac{\partial^2 P^{n+1}}{\partial x_j \partial x_j} = \frac{1}{\Delta t}\frac{\partial \tilde{u}_j^{n+1}}{\partial x_j}, \tag{11}$$

where $P = p + \frac{2}{3}k$.

(iii) The final velocity is calculated by including the pressure terms

$$u_i^{n+1} = \tilde{u}_i^{n+1} - \Delta t \frac{\partial P^{n+1}}{\partial x_i}. \tag{12}$$

(iv) After the final velocity components at the time $(n+1)\Delta t$ are obtained, k^{n+1} and ω^{n+1} are calculated by

$$\begin{aligned} k^{n+1} - \Delta t \frac{\partial}{\partial x_j}\left[\left(\nu + \sigma^* \nu_t^n\right)\frac{\partial k^{n+1}}{\partial x_j}\right] - \Delta t \tilde{k} \frac{\partial}{\partial x_k}\left(u_j^{n+1} u_k^{n+1} \frac{\partial k^{n+1}}{\partial x_j}\right) \\ = k^n + \Delta t\left(-u_j^{n+1}\frac{\partial k^n}{\partial x_j} + P_k^n - \beta^* \omega^n k^n\right), \end{aligned} \tag{13}$$

$$\begin{aligned} \omega^{n+1} - \Delta t \frac{\partial}{\partial x_j}\left[\left(\nu + \sigma \nu_t^n\right)\frac{\partial \omega^{n+1}}{\partial x_j}\right] - \Delta t \tilde{k} \frac{\partial}{\partial x_k}\left(u_j^{n+1} u_k^{n+1} \frac{\partial \omega^{n+1}}{\partial x_j}\right) \\ = \omega^n + \Delta t\left(-u_j^{n+1}\frac{\partial \omega^n}{\partial x_j} + \frac{\gamma \omega^n}{k^n} P_k^n - \beta(\omega^n)^2\right). \end{aligned} \tag{14}$$

In Eqs. (13) and (14), the parameter $\tilde{k}$ is evaluated at the time level $(n+1)\Delta t$ because the velocity at the time $(n+1)\Delta t$ has been obtained. However, the P_k is still evaluated at time level $n\Delta t$ because the turbulent viscosity at the the time level $(n+1)\Delta t$ is still unknown. The computational domain $\mathbf{\Omega}$ is divided into linear finite elements. The velocity components, pressure and the turbulence quantities in an element can be approximated as

$$u_i \approx \mathbf{N}\mathbf{U}_i,\ P \approx \mathbf{N}\mathbf{P},\ k \approx \mathbf{N}\mathbf{K},\ \omega \approx \mathbf{N}\mathbf{\Omega}, \tag{15}$$

where $\mathbf{N}$ is the shape function vector, $\mathbf{U}_i$, $\mathbf{P}$, $\mathbf{K}$ and $\mathbf{\Omega}$ represent the nodal values of u_i, P, k and ω, respectively. By selecting the shape function as the weighting function and applying a weighted residual formulation to Eqs. (10)–(14), one can obtains the following set of matrix equations:

$$\left[\mathbf{M} + \Delta t(\mathbf{D}^n + \mathbf{D}_u^n)\right]\tilde{\mathbf{U}}_i^{n+1} = \mathbf{M}\mathbf{U}_i^n + \Delta t \mathbf{C}^n \mathbf{U}_i^n, \tag{16}$$

$$\mathbf{S}\mathbf{P}^{n+1} = -\frac{1}{\Delta t}\mathbf{A}_i \tilde{\mathbf{U}}_i^{n+1}, \tag{17}$$

$$\mathbf{M}\mathbf{U}_i^{n+1} = \mathbf{M}\tilde{\mathbf{U}}_i^{n+1} - \Delta t \mathbf{A}_i \mathbf{P}^{n+1}, \tag{18}$$

$$\left[\mathbf{M} + \Delta t(\mathbf{D}^{n+1} + \mathbf{D}_k^n)\right]\mathbf{K}^{n+1} = \mathbf{M}\mathbf{K}^n + \Delta t\left(\mathbf{C}^{n+1}\mathbf{K}^n + \mathbf{F}_k^n\right), \tag{19}$$

$$\left[\mathbf{M} + \Delta t(\mathbf{D}^{n+1} + \mathbf{D}_\omega^n)\right]\mathbf{\Omega}^{n+1} = \mathbf{M}\mathbf{\Omega}^n + \Delta t\left(\mathbf{C}^{n+1}\mathbf{\Omega}^n + \mathbf{F}_\omega^n\right), \tag{20}$$

where

$$\mathbf{M}=\int_{\boldsymbol{\Omega}}\mathbf{N}^{\mathrm{T}}\mathbf{N}\,\mathrm{d}\boldsymbol{\Omega},\quad \mathbf{D}^n=\int_{\boldsymbol{\Omega}}\tilde{k}^n u_i^n u_j^n\frac{\partial\mathbf{N}^{\mathrm{T}}}{\partial x_i}\frac{\partial\mathbf{N}}{\partial x_j}\,\mathrm{d}\boldsymbol{\Omega},$$

$$\mathbf{A}_i=\int_{\boldsymbol{\Omega}}\mathbf{N}^{\mathrm{T}}\frac{\partial\mathbf{N}}{\partial x_i}\mathrm{d}\boldsymbol{\Omega},\quad \mathbf{S}=\int_{\boldsymbol{\Omega}}\frac{\partial\mathbf{N}^{\mathrm{T}}}{\partial x_i}\frac{\partial\mathbf{N}}{\partial x_i}\,\mathrm{d}\boldsymbol{\Omega},$$

$$\mathbf{D}_u^n=\int_{\boldsymbol{\Omega}}\left(v+v_t^n\right)\frac{\partial\mathbf{N}^{\mathrm{T}}}{\partial x_j}\frac{\partial\mathbf{N}}{\partial x_j}\mathrm{d}\boldsymbol{\Omega},\quad \mathbf{D}_k^n=\int_{\boldsymbol{\Omega}}\left(v+\sigma^*v_t^n\right)\frac{\partial\mathbf{N}^{\mathrm{T}}}{\partial x_j}\frac{\partial\mathbf{N}}{\partial x_j}\,\mathrm{d}\boldsymbol{\Omega},$$

$$\mathbf{D}_\omega^n=\int_{\boldsymbol{\Omega}}\left(v+\sigma v_t^n\right)\frac{\partial\mathbf{N}^{\mathrm{T}}}{\partial x_j}\frac{\partial\mathbf{N}}{\partial x_j}\mathrm{d}\boldsymbol{\Omega},\quad \mathbf{C}^n=\int_{\boldsymbol{\Omega}}-u_j^n\mathbf{N}^{\mathrm{T}}\frac{\partial\mathbf{N}}{\partial x_j}\,\mathrm{d}\boldsymbol{\Omega},$$

$$\mathbf{F}_k^n=\int_{\boldsymbol{\Omega}}\mathbf{N}^{\mathrm{T}}\left(P_k^n-\beta^*\omega^n k^n\right)\mathrm{d}\boldsymbol{\Omega},\quad \mathbf{F}_\omega^n=\int_{\boldsymbol{\Omega}}\mathbf{N}^{\mathrm{T}}\left(\frac{\gamma\omega^n}{k^n}P_k^n-\beta(\omega^n)^2\right)\mathrm{d}\boldsymbol{\Omega}.$$

Boundary integrations are not included in Eqs. (16)–(20) because they are replaced by the implementation of the boundary conditions on the boundaries of the computation domain. At the inflow boundary, a uniform nondimensional horizontal velocity distribution and zero transverse velocity are specified. The boundary conditions for the turbulent quantities are (Menter, 1993; Guilmineau and Queutey, 2004) $\omega_\infty=1$, $v_{t\infty}=10^{-3}$, $k_\infty=\omega_\infty v_{t\infty}$. At the cylinder surfaces, the logarithmic wall function is used (Brørs, 1999; Liang and Cheng, 2005). The first mesh node from the wall is set some distance (Δ_1) away from the cylinder surface. The gap between the cylinder surface and the mesh is bridged by the following logarithmic wall function:

$$\frac{u_T(y)}{u_*}=\begin{cases}\dfrac{yu_*}{v}, & \dfrac{yu_*}{v}\leqslant 11.63,\\[2ex] \dfrac{1}{\kappa}\ln\left(9\dfrac{yu_*}{v}\right), & \dfrac{yu_*}{v}>11.63,\end{cases}\tag{21}$$

where $u_T(y)$ is the velocity tangential to the cylinder surface, y is the distance from the wall, u_* is the friction velocity and κ is the von Karman constant ($=0.42$). In this study the distance between the mesh and the cylinder is set to be 0.5 times the mesh size in the normal direction of the boundary. The turbulent quantities at the wall boundary are specified as $k=C_\mu^{1/2}u_*^2$ and $\omega=k^{1/2}/(\beta^{*1/4}\kappa\Delta_1)$. At the two lateral boundaries, the transverse velocity component is set to be zero and a zero normal gradient condition is applied for all other quantities. At the outflow boundary, zero normal gradient of velocity, pressure and turbulence quantities are implemented. On the other boundaries, the pressure is obtained by applying the momentum equations in the direction normal to the boundaries.

The computational procedure can be briefly summarized as: (i) calculate the intermediate velocity according to Eq. (16); (ii) solve the pressure equation (Eq. (17)); (iii) calculate the final velocity by solving Eq. (18); (iv) calculate the turbulent quantities k and ω (Eqs. (19) and (20)); (v) calculate the turbulent viscosity according to Eq. (6); (vi) return to step (1) and repeat the procedure till the flow is fully developed.

4. Numerical results

4.1. Validation of the model

The computational model developed in this study is verified against uniform flow around an isolated single cylinder and uniform flow around two cylinders where independent experimental data are available. In the single cylinder case, the computational domain is divided into four-node linear finite elements. Calculations are carried out based on four meshes with different density (as shown in Table 2) in order to investigate the mesh dependence of the model. The mesh with medium density is shown in Fig. 2. The mesh quality for other meshes in Table 2 is similar to that given in Fig. 2 but with different mesh densities. The Reynolds number for the single cylinder case is $\mathrm{Re}=4.1\times10^4$. The computational time step is the same for all of the meshes and is taken as $\Delta t=0.002$.

The distributions of time-averaged pressure coefficient ($\bar{C}_p$) along the cylinder surface from the four meshes in Table 2 are plotted in Fig. 3. The C_p in Fig. 3 is defined as $C_p=(p-p_a)/(\rho U^2/2)$, with p_a being the pressure at the stagnation point of the cylinder and ρ being the fluid density. It can be seen that the pressure coefficient for fine mesh and that for finest mesh are almost identical. The predicted mean drag coefficient ($\bar{C}_D$), the root-mean-square (r.m.s.) lift coefficient (C_L') and the Strouhal number S_t are compared with the experimental data by Schewe (1983) and the numerical results

Table 2
Mesh properties for single cylinder case

Mesh density	Number of circumferential nodes	Grid size near the cylinder	Number of nodes in the mesh
Coarse	80	0.002	8155
Medium	120	0.0015	11920
Fine	160	0.001	13550
Finest	180	0.00075	15890

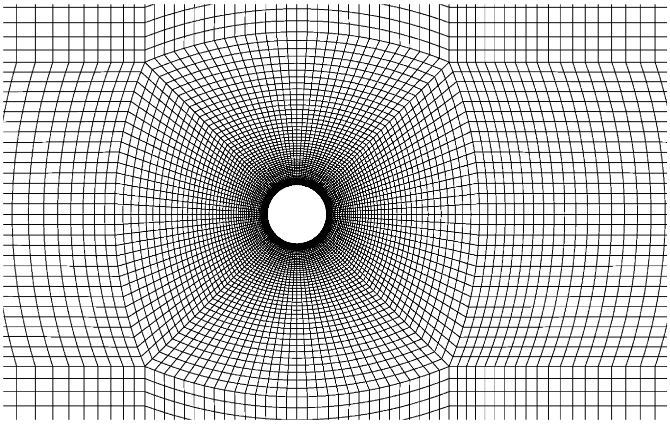

Fig. 2. Medium mesh for uniform past a single cylinder.

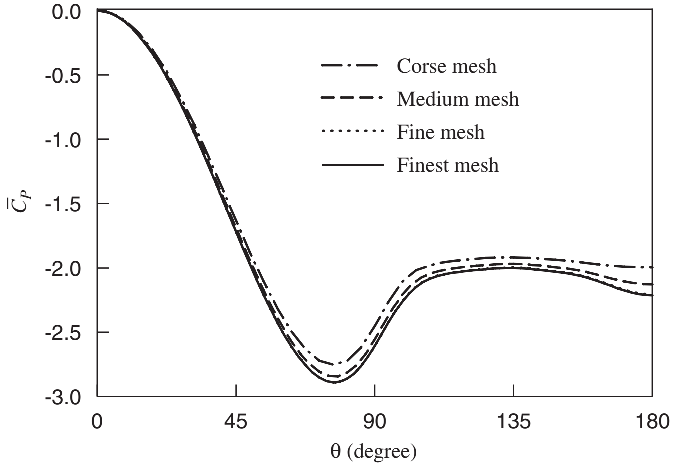

Fig. 3. Distribution of time-averaged pressure coefficient along the cylinder surface (Re = 4.1×10^4).

Table 3
Comparison of the force coefficient and Strouhal number (Re = 4.1×10^4)

Cases	Mean drag ($\bar{C}_D$)	R.m.s. lift (C'_L)	Strouhal number (S_t)
Coarse	1.002	0.472	0.220
Medium	1.044	0.596	0.220
Fine	1.068	0.655	0.217
Finest	1.078	0.667	0.211
Schewe (1983) (Re = 1–4 × 10^4)	1.15	0.35	0.20
Tsutsui et al. (1997) (Re = 4.1×10^4)	1.21		0.246

by Tsutsui et al. (1997) in Table 3. It can be seen that the present numerical results are almost mesh-independent on the fine mesh. The force coefficient and the Strouhal number change little when the mesh changes from the fine to the finest. The predicted mean drag coefficient and the Strouhal number agree well with the corresponding experimental values by Schewe (1983). The predicted r.m.s. lift coefficient (C'_L) of fine mesh is 0.655, which is larger than the measured value of 0.35 by Schewe (1983). However, the measured r.m.s. lift coefficient by So and Savkar, 1981 is around 1.0, which is larger than that computed in this study. It is stated (Tadrist et al., 1990; Lam et al., 2003) that the measured fluctuating forces are considerably affected by many factors, such as aspect ratio, blockage, turbulence intensity, tube end boundaries, etc. In all of the following study the mesh density around the cylinder surface is kept the same as the fine mesh of the single cylinder case.

Flow around two cylinders of different diameters is also simulated as a part of the validation of the present model. The cases investigated by Tsutsui et al. (1997) have a diameter ratio d/D of 0.45. The gap ratio between the two cylinders G/D is 0.0625. The Reynolds number based on the large cylinder diameter is $\mathrm{Re} = 4.1 \times 10^4$ and the Reynolds number based on the small cylinder is 1.845×10^4. The position angle α (defined in Fig. 1) ranges from 90° to 180° in the study by Tsutsui et al. (1997).

A rectangular computational domain with a length (in the flow direction) of $28D$ and a width of $16D$ is applied in the present study. This domain size was determined by a domain-size independence study. The centre of the large cylinder is located at $8D$ away from the inlet boundary and in the centre-line of the domain in the transverse direction. Fig. 4 shows the mesh near the cylinder for a typical case of $\alpha = 130^\circ$. The computational domain is discretized by 18 254 nodal points in the case of $\alpha = 130^\circ$. The perimeters of the large and small cylinders are discretized by 160 and 80 nodal points, respectively. The nondimensional element size in the radial direction next to the cylinders is around 0.001. The mesh characteristics near the cylinders for other cases investigated in this study are very similar to the case shown in Fig. 4. The nondimensional computational time step is 0.002 and the computation time is 250 for the two-cylinder cases.

Fig. 5 shows the comparison of the experimental and predicted distributions of mean pressure coefficient (C'_P) around the perimeter of large cylinder for cases of $\alpha = 90^\circ$, 120° and 160°. The pressure coefficient in Fig. 5 is defined by $C_p = (p - p_\infty)/(\rho U^2/2)$, where p_∞ is the pressure at the inlet. The numerical results by Tsutsui et al. (1997) are also included in the figures for the purpose of comparison. It can be seen from Fig. 5 that the predicted pressure distributions generally agree well with the experimental data and the numerical results of Tsutsui et al. (1997). However, obvious differences between the predicted and measured pressure distributions exist at around $\theta = -80^\circ$ and 90°, as can be seen from Fig. 5. Those locations seem to correspond to the locations of flow separation on the cylinder surface as the pressure gradient changes sign at those locations. Fig. 6 shows the comparison of the pressure coefficient distributions around the small cylinder for $\alpha = 90^\circ$, 120° and 160°. For the case of $\alpha = 90^\circ$, the front stagnation point on the small cylinder is located at around $\theta = -30^\circ$. This is because the incoming flow for the small cylinder is oblique to the x-axis. For the case of $\alpha = 160^\circ$, the pressure coefficient on the small cylinder is almost a constant, because the small cylinder is immersed in the wake of the large cylinder. It is seen from Figs. 5 and 6 that the present numerical results agree slightly better with the experimental results than those by Tsutsui et al. (1997), especially at the rear of the large cylinder. This is likely because of the finer grid resolution used in this study.

Figs. 7 and 8 show the comparisons of the predicted and measured mean drag and mean lift coefficients on the large cylinder and those on the small cylinder, respectively, for different values of α. It can be seen that the present numerical results agree reasonably well with the experimental data. The dependence of the drag and lift coefficients on the position angle α is well captured by the numerical model. The computed mean drag coefficient on the large and small cylinders is slightly smaller than its measured counterpart while the computed mean lift coefficient is slightly larger than its measured counterpart for almost all the position angles investigated in this study. Fig. 9 shows the comparison of the predicted and measured values of Strouhal number. The Strouhal number is obtained by Fourier transforming the total lift on the cylinder bundle. The experiments conducted by Tsutsui et al. (1997) detected two distinct values of Strouhal number corresponding to a single value of position angle α when α is between 90° and 130°. It was stated (Tsutsui et al., 1997) that the lower values of the pairs correspond to the so-called reattachment state (as will be discussed in the next section). The same phenomenon was also observed in the present numerical study in the region of $\alpha = 90^\circ$–120°. It can be seen from Fig. 9 that the higher values of the pairs agree well with the measured data, whereas the lower values of the pairs are smaller than those measured.

4.2. Effects of position angle α and gap ratio G/D

The effects of the gap ratio and position angle of the small cylinder on the vortex shedding from the two cylinders and the forces on the two cylinders are studied by a series of numerical tests. The numerical tests were conducted for a diameter ratio of $d/D = 0.5$, the large cylinder Reynolds number of 5×10^4 and gap ratio of 0.05, 0.1, 0.2, 0.4 and ∞. The small cylinder Reynolds number is 2.5×10^4. The position angle of the small cylinder (α) ranges from 0° to 180°

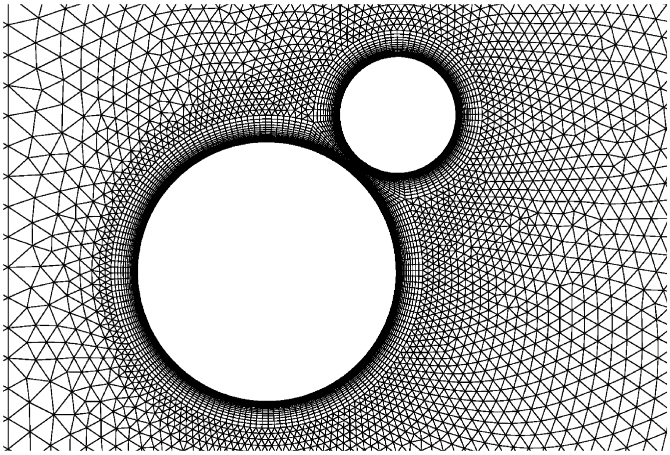

Fig. 4. A typical computational mesh near the cylinders ($G/D = 0.1$, $d/D = 0.45$, $\alpha = 130°$).

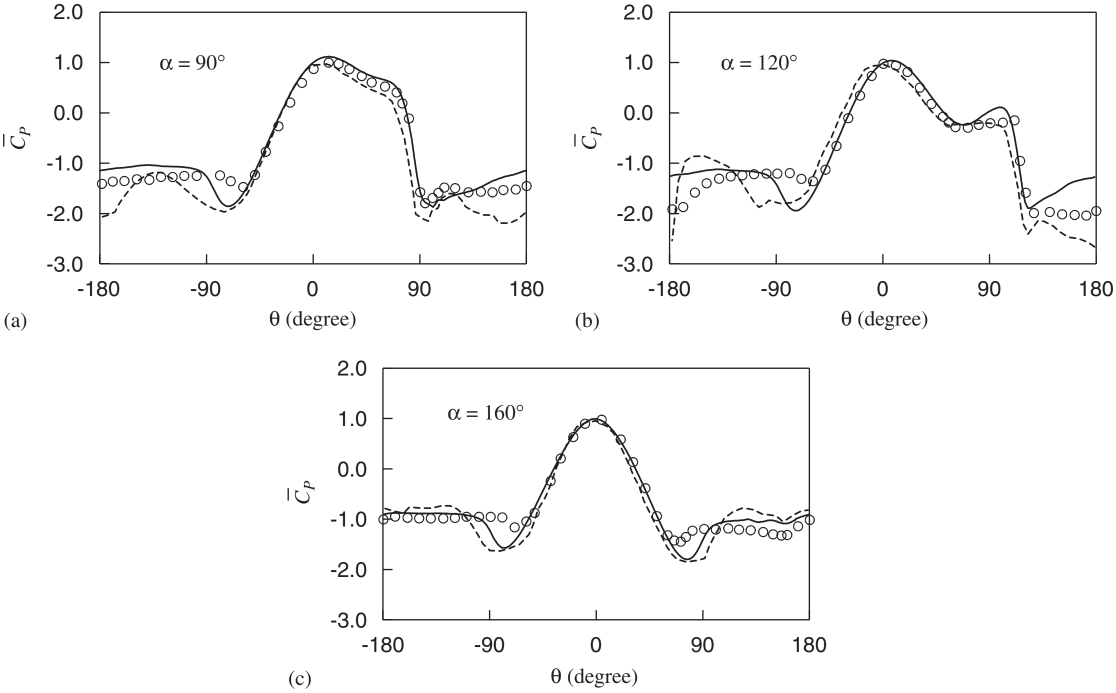

Fig. 5. Mean pressure coefficient distributions along the large cylinder ($Re = 4.1 \times 10^4$): ○, experimental (Tsutsui et al., 1997); - - - - -, numerical (Tsutsui et al., 1997); ——, present.

with an interval of 22.5°. The computed fluctuating force coefficients and the Strouhal number are compared with those of a single isolated cylinder at the same Reynolds number. The perimeters of the large and small cylinders are discretized by 160 and 80 nodal points, respectively. The mesh quality in this section is similar to that shown in Fig. 4. The computational time step is set to be 0.002. The force coefficients on an isolated single cylinder in a uniform flow at $Re = 5 \times 10^4$ and 2.5×10^4 are calculated for the purpose of comparison. In the singular cylinder calculation, the cylinder perimeter is discretized using 160 nodal points for $Re = 5 \times 10^4$ and 80 nodal points for $Re = 2.5 \times 10^4$ in order to ensure that the mesh has the same density as in the dual cylinder case. The computed force coefficients and the Strouhal numbers are listed in Table 4. It can be seen from Table 4 that the differences between the results for $Re = 5 \times 10^4$ and 2.5×10^4 are insignificant.

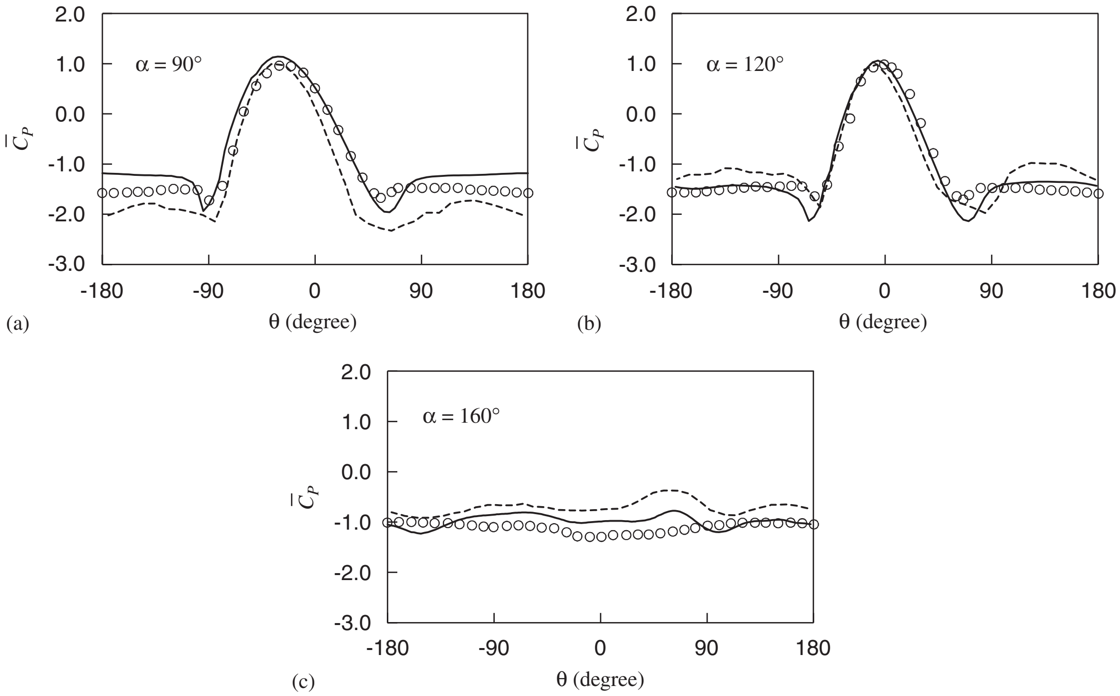

Fig. 6. Mean pressure coefficient distributions along the small cylinder (Re = 1.845×10^4): ○, experimental (Tsutsui et al., 1997); -----, numerical (Tsutsui et al., 1997); ——, present.

4.2.1. Force coefficients

Fig. 10 shows the variation of mean force coefficients on the large cylinder and those on the small cylinder. It can be seen that the mean drag coefficient on the large cylinder attains its maximum value when the two cylinders are in near side-by-side arrangement (α is around 90°) for all values of G/D. The maximum mean drag on the large cylinder increases with the decrease of G/D. The drag on the large cylinder for $G/D = 0.05$ and $\alpha = 90°$ is about 1.5 times that on a single isolated cylinder. The drag increase for the near side-by-side arrangements (α is around 90°) is mainly caused by the increases of the stagnation pressure and the high-pressure area in front of the cylinder. This can be seen clearly by examining the mean pressure distributions on the surface of the large cylinder given in Fig. 17. The mean drag on the large cylinder is smaller than its single cylinder counterpart when the two cylinders are in near tandem arrangements ($0° < \alpha < 45°$ and $135° < \alpha < 180°$). The drag reduction is mainly caused by the combination of a decrease in the stagnation pressure and an increase of the base pressure of the large cylinder (see Fig. 17), when the small cylinder is placed in front of the stagnation point of the large cylinder (α is around 0°). The drag reduction is mainly induced by the increase of base pressure of the large cylinder (see Fig. 17) when the small cylinder is placed in the wake region of the large cylinder (α is around 180°). The base pressure increase of the large cylinder for the near tandem arrangements is due to the disturbances of the small cylinder to the formation of the upper shear layer of the large cylinder (α is around 0°) and the interactions of the shear layers of the large cylinder (α is around 180°) (Sakamoto and Haniu, 1994). The drag reductions observed for the near tandem arrangements is more understandable intuitively, because the placement of a small cylinder in front of the large cylinder is effectively equivalent to attaching a streamlined nose to the large cylinder, and a small cylinder at the back equivalent to attaching a streamlined tail to the large cylinder. The mean lift on the large cylinder is negative when the cylinders are in near side-by-side arrangements and positive when the cylinders are in near tandem arrangements. It is seen that the maximum absolute mean lift on the large cylinder occurs when α is around 112.5°. The absolute values of the mean lift on the large cylinder increase with the decrease of the gap ratio G/D.

It can be seen from Fig. 10(c) that the mean drag on the small cylinder is insensitive to the values of the gap ratio G/D. However, the angle α does affect the mean drag on the small cylinder very much. The mean drag is around 0.5 for $\alpha = 0°$. It increases with the increase of α until α is around 45° or 67.5°. Further increase of α induces a decrease of the mean drag on the small cylinder. The mean drag on the small cylinder is negative for $\alpha = 80°$ in the computed cases of G/D. From Fig. 10(d) it can be seen the effect of the gap ratio on the mean lift on the small cylinder is significant,

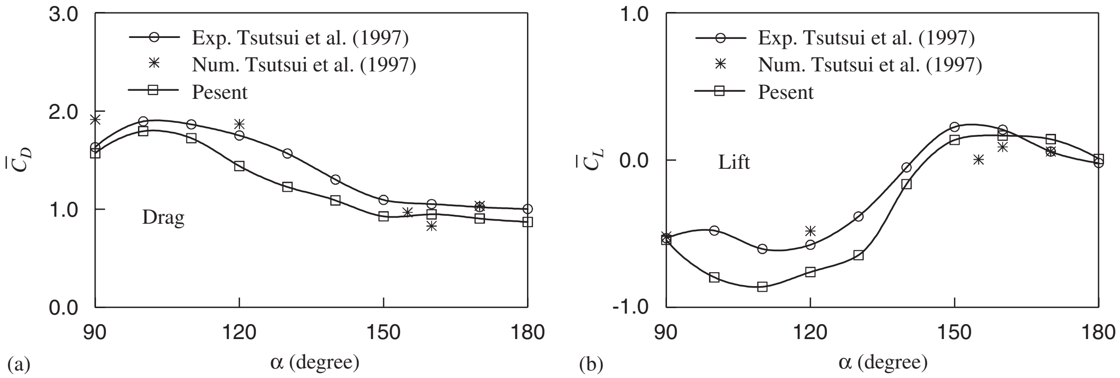

Fig. 7. Variation of the mean force coefficient on large cylinder with α (Re = 4.1×10^4).

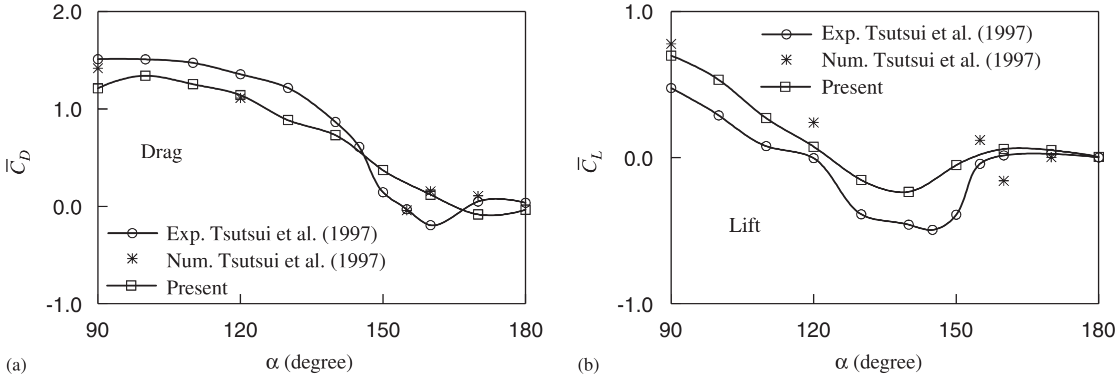

Fig. 8. Variation of mean force coefficient on small cylinder with α (Re = 1.845×10^4).

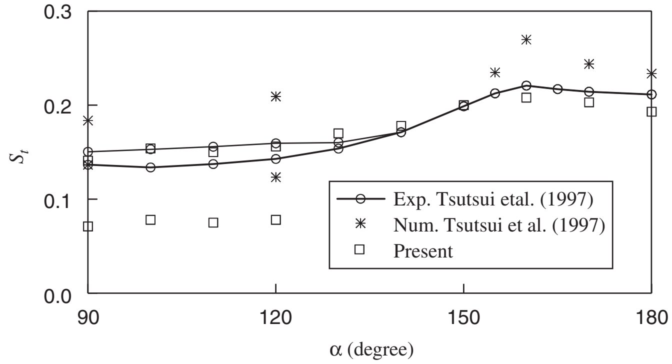

Fig. 9. Variation of the Strouhal number with α (large cylinder Re = 4.1×10^4).

Table 4
Computed force coefficients and the Strouhal number for a single cylinder

Reynolds number (Re)	Mean drag ($\bar{C}_D$)	Mean lift ($\bar{C}_L$)	R.m.s. drag (C'_D)	R.m.s. lift (C'_L)	Strouhal number (S_t)
5×10^4	1.084	0	0.038	0.623	0.207
2.5×10^4	1.044	0	0.035	0.605	0.217

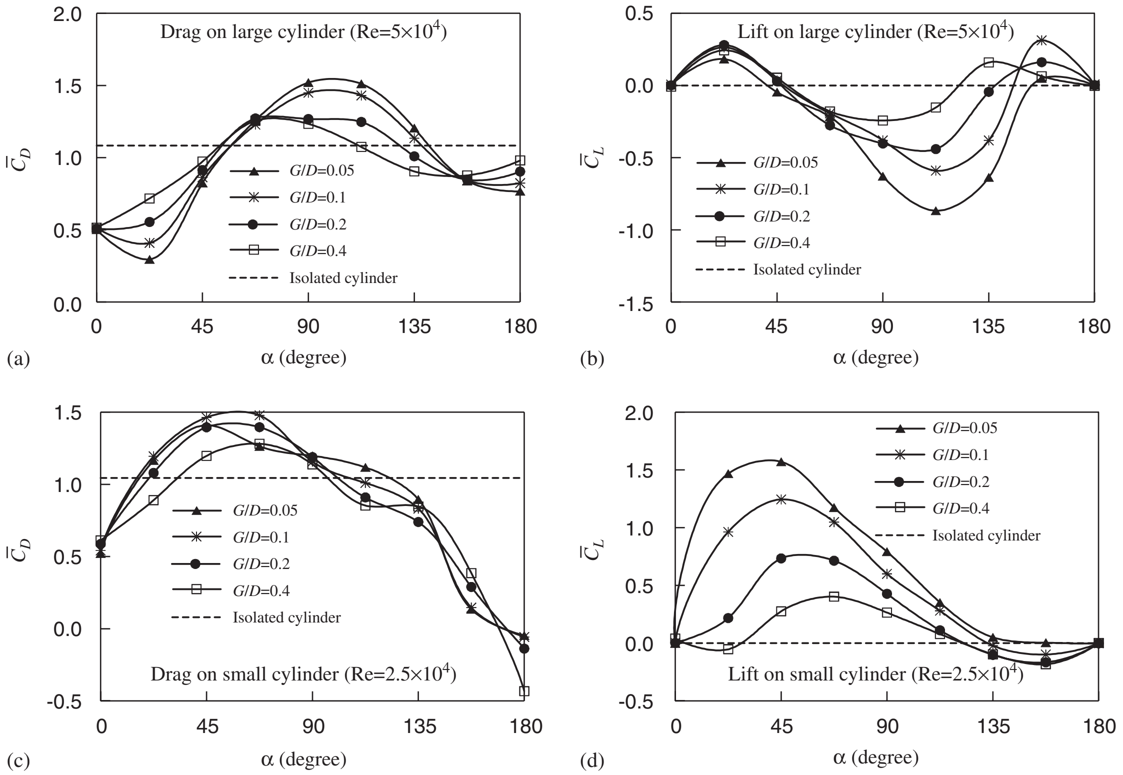

Fig. 10. Variation of mean force coefficients with α.

especially when the small cylinder is in the upstream side of the large cylinder ($\alpha < 0$ 90°). The mean lift on the small cylinder is positive for $\alpha < 135°$ and negative for $\alpha > 135°$. For $G/D = 0.05$ and 0.1, the mean lift on the small cylinder is zero when $\alpha = 0°$; it increases sharply to large values when α is increased a little, as shown in Fig. 10(d). The maximum mean lift on the small cylinder takes place when α is around 45° for most of the gap ratios investigated in the present study.

Fig. 11 shows the distribution of the mean force coefficient vector plots $\bar{\boldsymbol{C}}_F = (\bar{C}_D, \ \bar{C}_L)$, following the same approach by Zdravkovich (1977). The force vectors given in Fig. 11 are plotted using the coordinates (G, α) that represent the relative location of the small cylinder to the large cylinder. The force vectors plotted in Fig. 11(a) are those acting on the large cylinder, while the force vectors shown in Fig. 11(b) are those acting on the small cylinder. It is seen that the absolute value of the mean force on the large cylinder attains its maximum value when the small cylinder is very close to the large one and the angle α is between 90° and 112.5°. In the case of $G/D = 0.05$, the absolute values of the force vector at $\alpha = 90°$ and 112.5° are 1.65 and 1.75, respectively, which are 1.52 and 1.62 times of the mean drag coefficient on an isolated single cylinder, respectively. The existence of the small cylinder also affects the direction of the mean force coefficient on the large cylinder. The maximum absolute value on the small cylinder occurs at $G/D = 0.05$ and $\alpha = 45°$, and its value is about 2.96, which is 2.74 times of the mean drag on a single cylinder. The absolute value of the force on the small cylinder approaches to zero when the small cylinder is located in the wake of the large cylinder.

Fig. 12 shows the variation of the time-averaged total drag coefficient ($\bar{C}_{DE}$) and total lift coefficient ($\bar{C}_{LE}$) on the two-cylinder system, which are based on the so-called equivalent diameter ($D_e = D + d + G$). The mean total drag coefficients in Fig. 12(a) are normalized by the mean drag coefficients on an isolated cylinder at $\mathrm{Re} = 5 \times 10^4$ ($\bar{C}_{D0}$). It is seen from Fig. 12(a) that the variation of the mean total drag coefficient is more or less the same to that of the mean drag on the large cylinder. The mean total drag coefficient is about 0.5 times that on an isolated cylinder when $\alpha = 0°$ and 180°. It increases when the small cylinder moves from the front or the rear of the large cylinder to its side. The total drag coefficient increases when the gap ratio decreases. The total drag is larger than that on a single cylinder when α is around 90° and G/D is very small ($G/D = 0.05$ and 0.1 in Fig. 12(a)). It is seen that the variation of the mean total lift coefficient is different from either that on the large or the small cylinder. The mean total lift coefficient attains its maximum value when α is around 135° or 157.5°, and its minimum value when α is around 67.5°. The magnitudes of the mean total lifts for the computed G/D are very small when the two cylinders are in a near side-by-side arrangement ($\alpha = 90^\circ$). The absolute value of the mean total lift coefficient increases when the gap ratio G/D decreases. Fig. 13 shows the variation of the time-averaged total drag coefficient ($\bar{C}_{DA}$) and total lift coefficient ($\bar{C}_{LA}$) on the two-cylinder system, which are based on the sum of the two-cylinder diameter ($D_A = D + d$). The variation of the force coefficients $\bar{C}_{DA}$ and $\bar{C}_{LA}$ with G/D and α reflect the effects of the small cylinder position on the dimensional total force because they are based on a dimension independent of both α and G/D. Because $D_E > D_A$, the absolute value of the force coefficients in Fig. 13 for a given G/D and α generally larger than their counterparts in Fig. 12. However, it can be seen by comparing Figs. 12 and 13 that the variation of the $\bar{C}_{DA}$ and $\bar{C}_{LA}$ with α are quite similar to those of $\bar{C}_{DE}$ and $\bar{C}_{LE}$, respectively. It can be seen from Figs. 12 and 13 that the mean total lift changes from a positive value sharply to a large negative value when α increases from 22.5° to 45°. A large reduction also occurs when α increases from 157.5° to 180° for $G/D = 0.05$ and 0.1.

Fig. 14 shows the variation of the root-mean-square (r.m.s.) drag and lift coefficients (C'_D and C'_L) on the large cylinder and those on the small cylinder with the position angle α. The r.m.s. drag coefficient on the large cylinder is smaller than that of an isolated cylinder when the small cylinder is located in the front of or at the rear of the large cylinder and larger when the small cylinder is at the side of the large cylinder. The r.m.s. lift on the large cylinder is almost always smaller than that on an isolated cylinder. Significant r.m.s. lift reductions take place when the small cylinder is placed either in the wake of or in front of the large cylinder. This is likely caused by the disturbances of the small cylinder to the formation of the shear layers at the upstream face of the large cylinder and the interaction of the shear layers in the wake region of the large cylinder, as discussed earlier on. The r.m.s. drag coefficient on the small cylinder is much larger than that on an isolated cylinder at the same Reynolds number for α around 30–60° and 120–150°. From Fig. 14(d) it can be seen that the r.m.s. lift on the small cylinder is much smaller than that on an isolated cylinder consistently, especially when the small cylinder is located in front of the large cylinder.

Fig. 15 shows the contours of the r.m.s. force coefficients ($C'_F = \sqrt{(C'_D)^2 + (C'_L)^2}$) on each cylinder as the function of the position of small cylinder centre. When $\alpha = 45^\circ$ and $G/D = 0.2$, the C'_F of the large cylinder attains its maximum value. The existence of a small cylinder in the wake of a large one hinders the interaction of the shear layer behind the large cylinder. This leads to the reduction of the r.m.s. force coefficient at large values of α as shown in Fig. 15(a). However the interaction of the shear layer from the large cylinder causes the r.m.s. force coefficient on the small cylinder to increase when the small cylinder is moved from the front to the rear of the large cylinder as shown in Fig. 15(b). The maximum values of C'_F on the small cylinder occurs when $\alpha = 135^\circ$ and $G/D = 0.05$.

Fig. 16 shows the r.m.s. of the total force coefficients on the two-cylinder system based on the equivalent diameter (D_E). The r.m.s. total drag coefficient and r.m.s. total lift coefficient are normalized by those on an isolated cylinder $\left(C'_{D0}\text{ and }C'_{L0}\right)$ at $\mathrm{Re} = 5 \times 10^4$, respectively. It is seen that the C'_{DE} is larger than that of an isolated cylinder when α between 90° and 112.5° for $G/D = 0.2$ and 0.4, when α is between 45° and 112.5° for $G/D = 0.1$, and when α between 45° and 90° for $G/D = 0.05$. It is seen from Fig. 16(b) that C'_{LE} is always smaller than that on an isolated cylinder, regardless of the gap ratio G/D and the angle α. When α is around 135°, the r.m.s. total lift attains its maximum value of about 0.5–0.65 times that on an isolated cylinder.

4.2.2. Pressure coefficient distributions

Fig. 17 shows the distribution of the time-averaged pressure coefficients ($\bar{C}_p$) along the perimeter of the large cylinder with the position angle of the small cylinder at two typical gap ratios investigated. It can be seen that the existence of the small cylinder affects the mean pressure distribution on the large cylinder. By comparing Fig. 17(a) and (b), it can be seen that the effect of the small cylinder is significant when the small cylinder is close to the large one, especially when the small cylinder is located at about the side of the large cylinder ($\alpha = 45^\circ$, 90° and 135° in Fig. 17). The pressure distributions on the large cylinder surface are more asymmetric for the small value of G/D than those for the large value of G/D. This may be one of the reasons for the large values of mean lift force on the large cylinder at small values of G/D as shown in Fig. 10(b). Due to the existence of the smaller cylinder in front of the large one for $\alpha = 0^\circ$, the pressure in front of the large cylinder ($\theta = 0^\circ$) reduces much more, compared to that for an isolated cylinder. The reduction of the pressure in front of the large cylinder leads to a smaller mean drag force on the large cylinder (as shown in Fig. 10(a)).

Fig. 18 shows the time-averaged pressure coefficients along the perimeter of the small cylinder. It can be seen that the pressure distribution on the small cylinder is more strongly affected by the location of the small cylinder than that on the large cylinder. This is mainly because the approaching flow conditions for the small cylinder are very different when it is located at different relative positions to the large cylinder. For example, at $\alpha = 180^\circ$, the pressure coefficient on the small cylinder is almost a negative constant, because the whole cylinder is immersed in the wake of the large cylinder. It is also seen that the pressure distributions are symmetric when the small cylinder is located on the symmetric line at

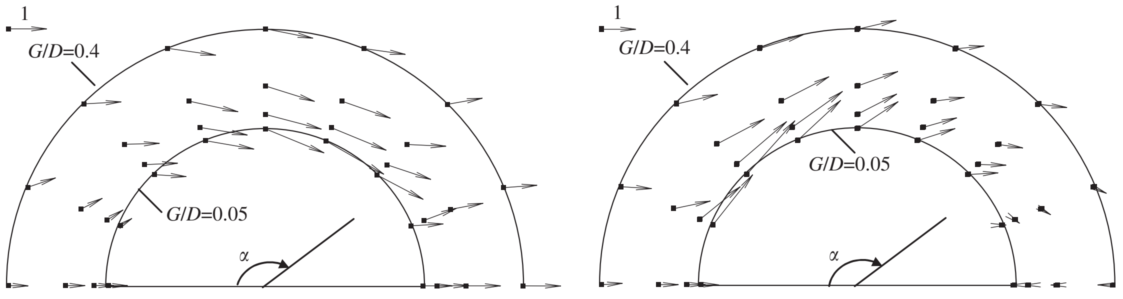

(a) Large cylinder (Re=5×10^4) (b) Small cylinder (Re=2.5×10^4)

Fig. 11. Mean force coefficient vector on cylinders.

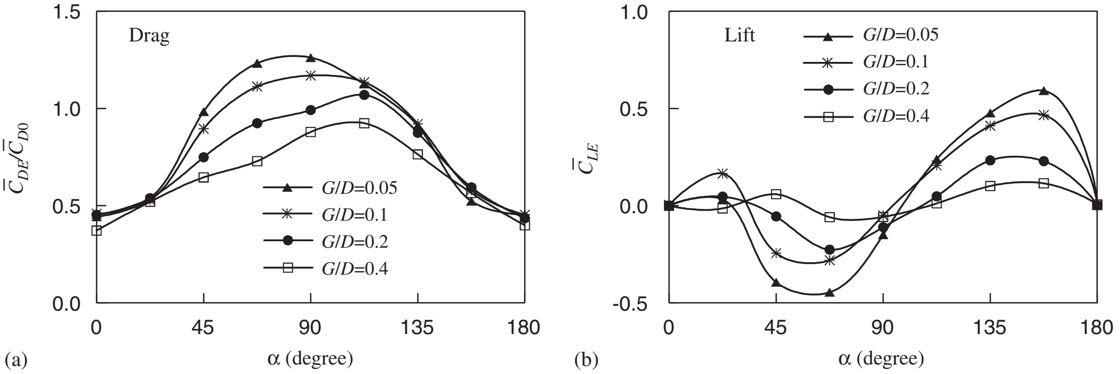

Fig. 12. Time-averaged total force coefficients based on the equivalent diameter ($D_e = D + d + G$) (large cylinder Re $= 5 \times 10^4$).

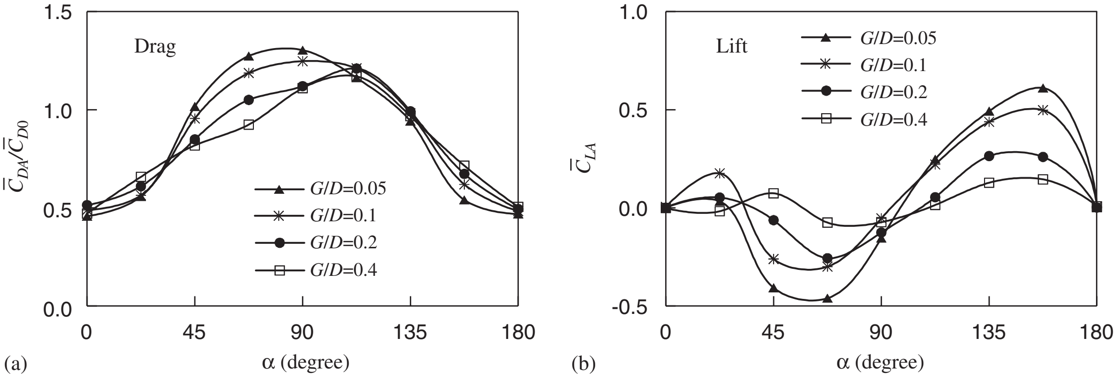

Fig. 13. Time-averaged total force coefficients based on the sum of the cylinder diameter ($D_A = D + d$) (large cylinder Re $= 5 \times 10^4$).

$\alpha = 0^\circ$ and 180°. For other cases, the pressure distribution is asymmetric. The pressure distribution is more asymmetric when $\alpha < 90^\circ$ than that when $\alpha > 90^\circ$. This is the reason that the lift on the small cylinder for $\alpha < 90^\circ$ is larger than that for $\alpha > 90^\circ$ (as shown in Fig. 10(d)). The stagnation point on the small cylinder is located at the lower side of the cylinder as $\alpha < 90^\circ$. This leads to a positive lift force on the small cylinder.

4.2.3. *Vortex flow patterns*

It is expected that the shedding process from the cylinders is dependent on the location of the small cylinder. It is observed that vortex shedding characteristics for the two-cylinder case are similar to those from a single cylinder when

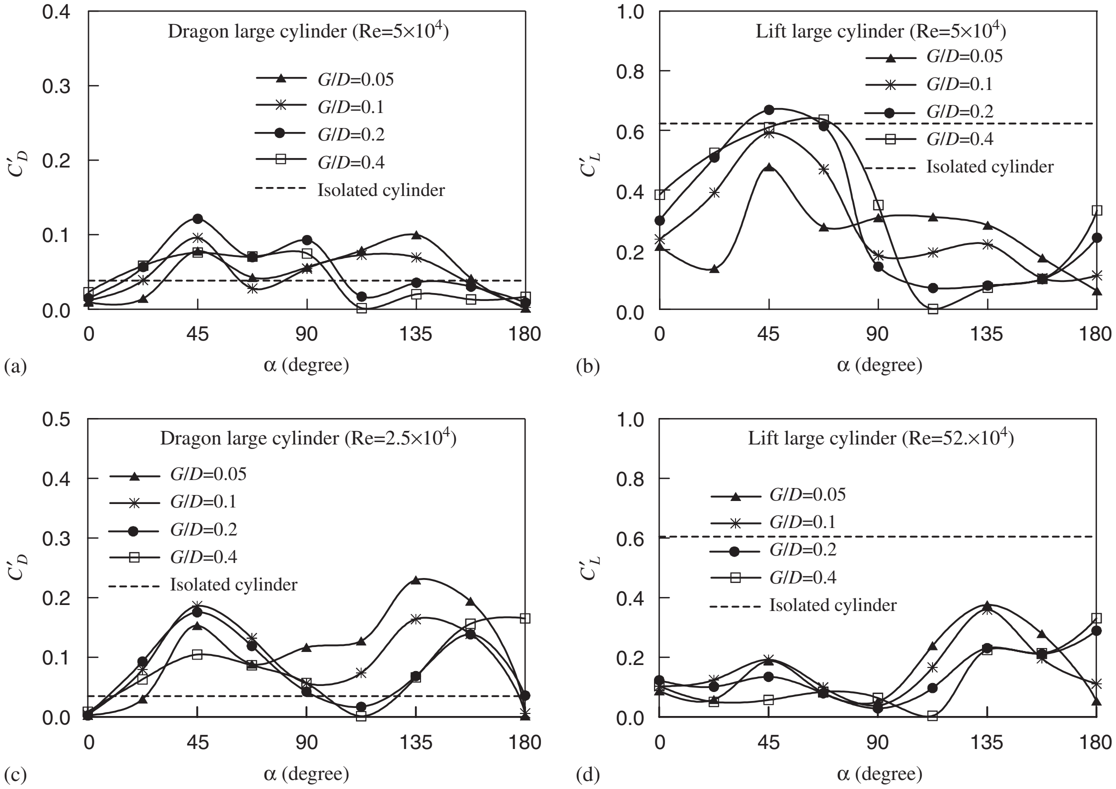

Fig. 14. Root-mean-square force coefficients on the cylinders.

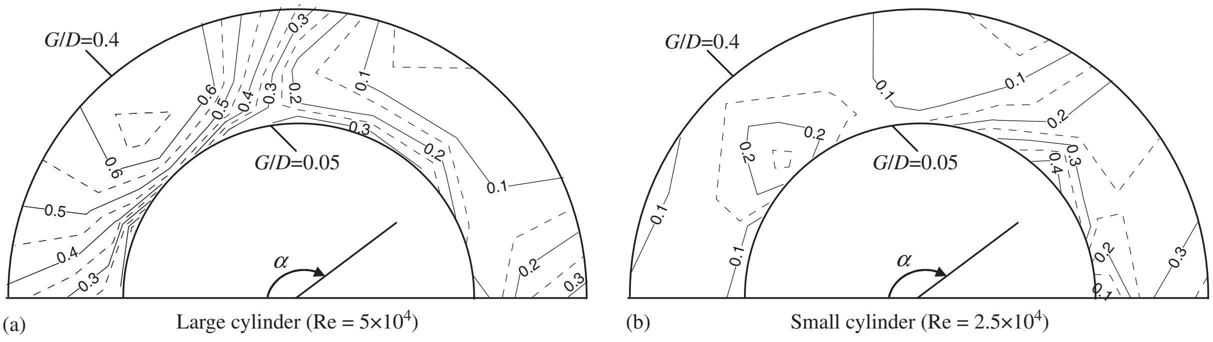

Fig. 15. Contour of the r.m.s. force coefficients $C'_F = \sqrt{(C'_D)^2 + (C'_L)^2}$.

the gap between the cylinders is small. There is only one vortex shedding wake behind the cylinders in this case. The critical gap ratio, below which the two cylinders behave as a single body, is dependent on the position angle α of the small cylinder. Fig. 19 shows the power spectra of the total lift coefficient on the two cylinders for $G/D = 0.1$ and different values of α. For $G/D = 0.1$, the lift on the two-cylinder bundle is found to oscillate at a single frequency, except for $\alpha = 90^\circ$ and 112.5°. It is quite obvious that there exists only one dominant vortex shedding frequency for these position angles at this particular gap ratio. It can be seen from Fig. 19 that the power spectra have two sharp peaks for $\alpha = 90^\circ$ and 112.5°. This suggests that there exist two shedding processes for those two cases.

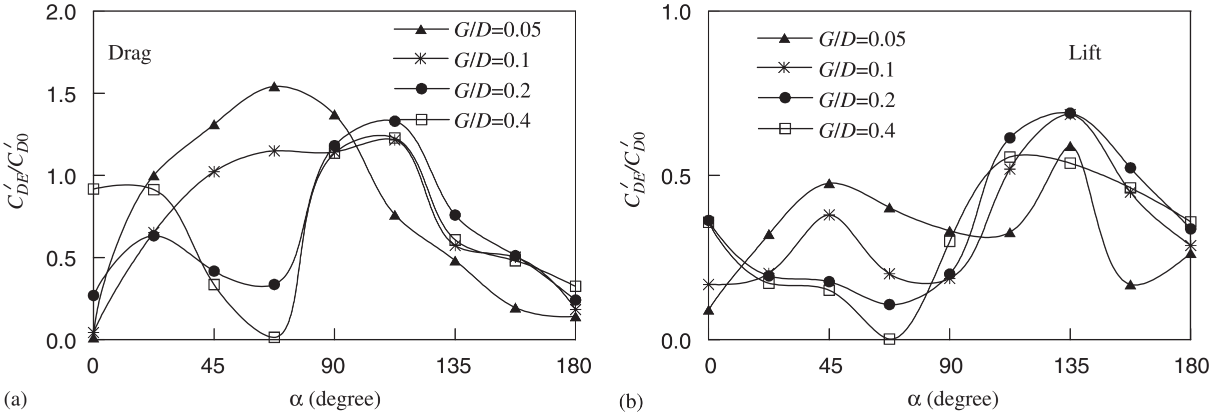

Fig. 16. Root-mean-square of the total force coefficients based on the equivalent diameter ($D_e = D + d + G$) (large cylinder $\mathrm{Re} = 5 \times 10^4$).

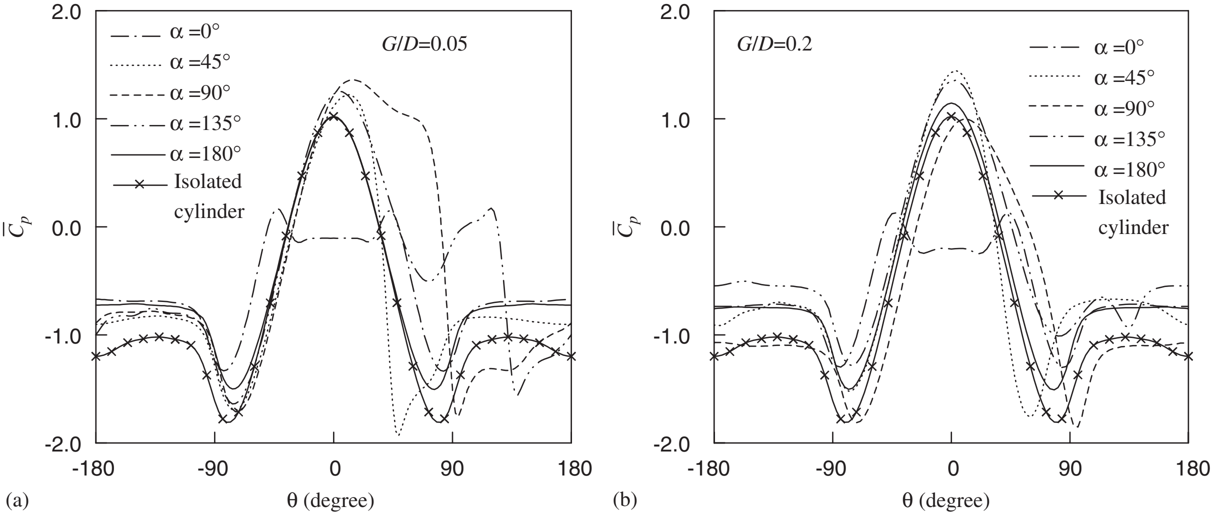

Fig. 17. Mean pressure coefficient distributions along the large cylinder ($\mathrm{Re} = 5 \times 10^4$).

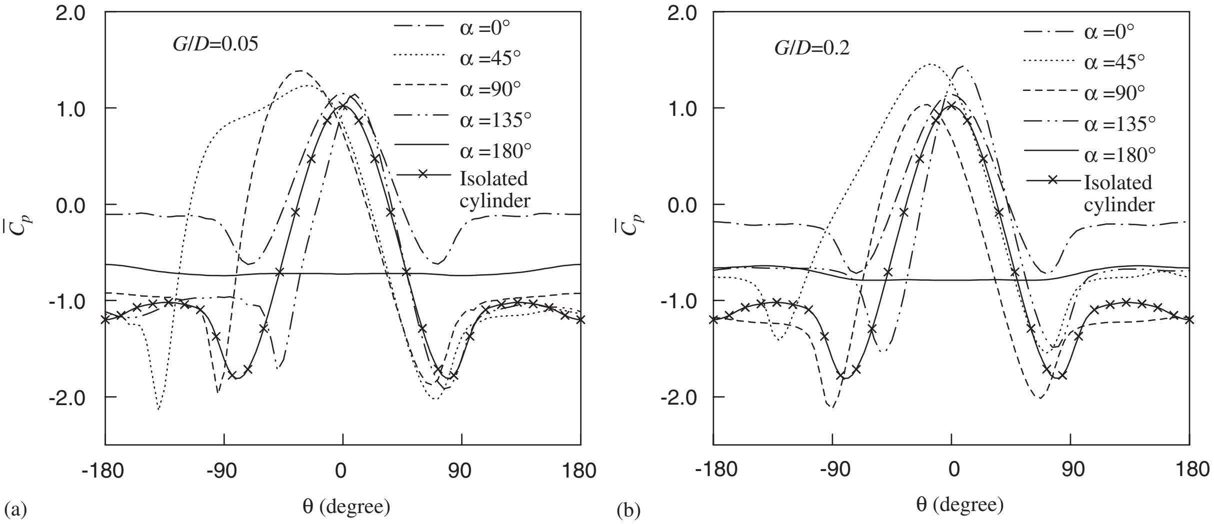

Fig. 18. Mean pressure coefficient distributions along the small cylinder ($\mathrm{Re} = 2.5 \times 10^4$).

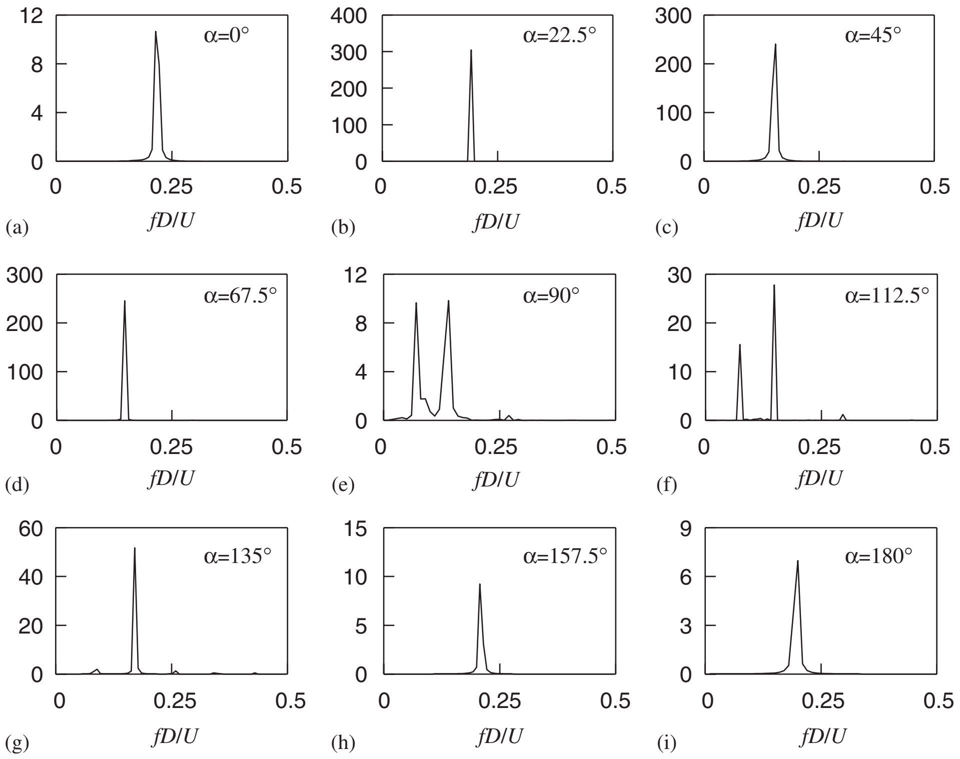

Fig. 19. Power spectra of the total lift coefficients for G/D = 0.1 (large cylinder Re = 5×10^4).

Fig. 20 shows the instantaneous contours of vorticity (defined as $\omega_s = \partial u_2/\partial x_1 - \partial u_1/\partial x_2$) behind the two cylinders for $G/D = 0.1$ and $\alpha = 67.5°$ from dimensionless time $Ut/D = 150$–156.5, which is about one shedding period. The solid lines represent the positive vorticity and the dashed ones represent the negative vorticity. The wake behind the cylinders is one of the typical characteristics of the vortex shedding from an isolated body. The shear layers from the upper side of the small cylinder and that from the lower side of the large cylinder interact behind the cylinders, forming a typical vortex street. The shear layers from the gap between the cylinders do not interact actively and the flow pattern behind the gap nearly remains stationary during the shedding period. The Strouhal number based on the large cylinder diameter of the vortex shedding is 0.148 for $G/D = 0.1$ and $\alpha = 67.5°$, which is smaller than that of a single cylinder. Fig. 21 shows the time histories of the drag and lift coefficients on the two cylinders for $G/D = 0.1$ and $\alpha = 67.5°$. It can clearly be seen that the drag and the lift coefficients on both two cylinders oscillate at a same frequency. This is referred to as one-wake mode.

Fig. 22 shows the instantaneous vorticity contours behind the two cylinders for $G/D = 0.1$ and $\alpha = 112.5°$. The flow patterns in Fig. 22 qualitatively agree with the observed ones in the experiments by Tsutsui et al. (1997). From Fig. 22(a–c), one can see that the separated shear layer from the large cylinder reattaches to the rear face of the large cylinder, forming a wall jet. It is observed that the flow in the rear of the gap is biased to the rear face of the large cylinder. Tsutsui et al. (1997) called this phenomenon "reattachment". On the other hand, in Fig. 22(d) and (e), it is observed that the separated shear layer through the gap detaches from the rear face of the large cylinder and form a free jet. The reattachment re-occurs at the moment $Ut/D = 160$ (Fig. 22(f)). It is observed that the reattachment of the separated shear layer occurs intermittently. The intermittent reattachment of the shear layer affects the force on the cylinders very much. Fig. 23 shows the time history of the force coefficients on the two cylinders for $G/D = 0.1$ and $\alpha = 112.5°$. It is obvious that the force coefficients in Fig. 23 oscillate in multiple frequencies. The force coefficients are composed of a high-frequency component superposed on a low-frequency one, as observed in Fig. 19(e) and (f). The lower values of the Strouhal number in Fig. 19(e) and (f) correspond to the frequency of the reattachment. The shear layers from the large cylinder and those from the small cylinder interact with each other. The vortex shedding behind the cylinders is affected by the shear layer behind the gap. This mode is referred to as the interaction-shedding mode.

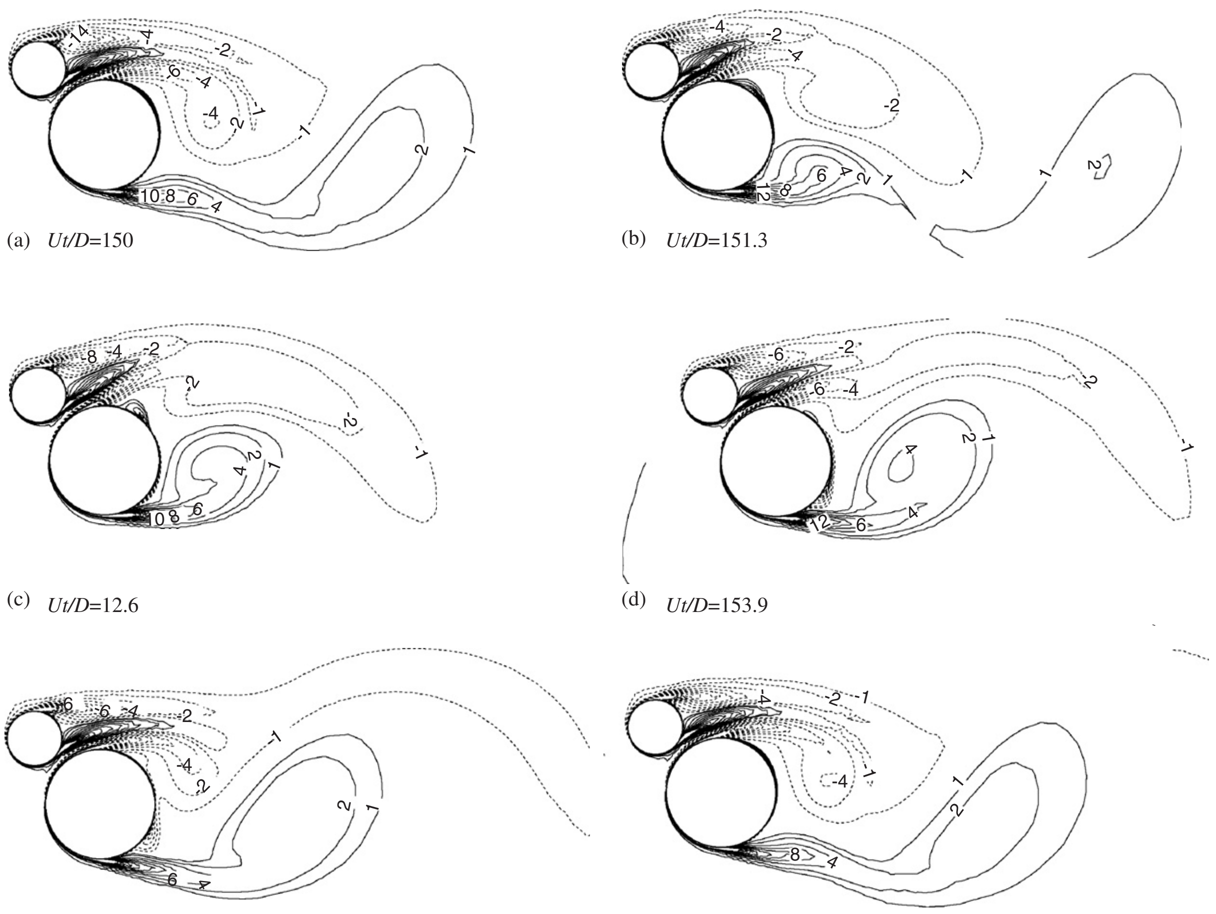

(a) *Ut/D*=150 (b) *Ut/D*=151.3

(c) *Ut/D*=12.6 (d) *Ut/D*=153.9

(e) *Ut/D*=15.2 (f) *Ut/D*=155.5

Fig. 20. Instantaneous vorticity contours behind the two cylinders for $G/D = 0.1$ and $\alpha = 67.5^\circ$ (large cylinder $\mathrm{Re} = 5 \times 10^4$).

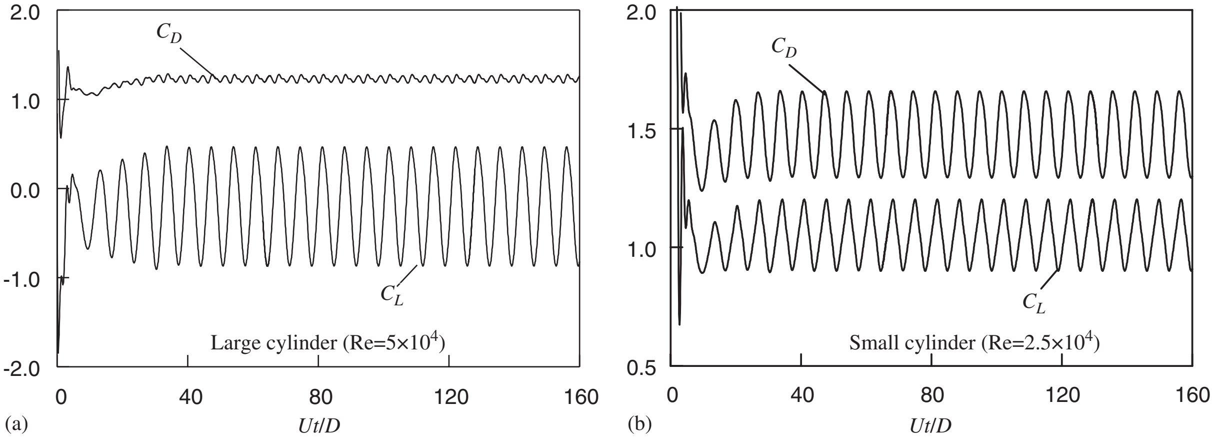

Fig. 21. Time history of the force coefficients on the two cylinders for $G/D = 0.1$ and $\alpha = 67.5^\circ$.

It is observed that the one-wake mode occurs as the angle α is near 0° or near 180° or when the small cylinder is located in the front side of the large cylinder, whereas the interaction-shedding mode occurs as small cylinder is located in the rear side of the large cylinder. The range of the angle α in which the interaction-shedding mode occurs is between

90° and 112.5° for $G/D = 0.1$. It is found that this range of the angle α is different for different gap ratio G/D. It is observed that this range expands as the gap ratio G/D increases.

4.2.4. Shedding frequency

The Strouhal number of the lift on the two cylinders is studied. The variations of the Strouhal number of the lift with the angle α for different gap ratio G/D are plotted in Fig. 24. The Strouhal number for the small, large and isolated cylinders is based on their diameters correspondingly. For some cases, the power spectra of the lift may have several sharp peaks (as shown in Fig. 19(e) and (f)). In these cases, all values of the Strouhal number are plotted in Fig. 24. For $\alpha < 67.5°$ and $\alpha > 157.5°$, both the large cylinder and the small cylinder have a single Strouhal number, and the Strouhal number of the large cylinder is twice of that of the small cylinder. This means that the lift on the large cylinder and that on the small cylinder oscillate in an identical dimensional frequency and hence the two cylinders act as a single body in these cases. In the cases of α between 90° and 135°, the fluctuation of the lift coefficient has multiple frequencies. This

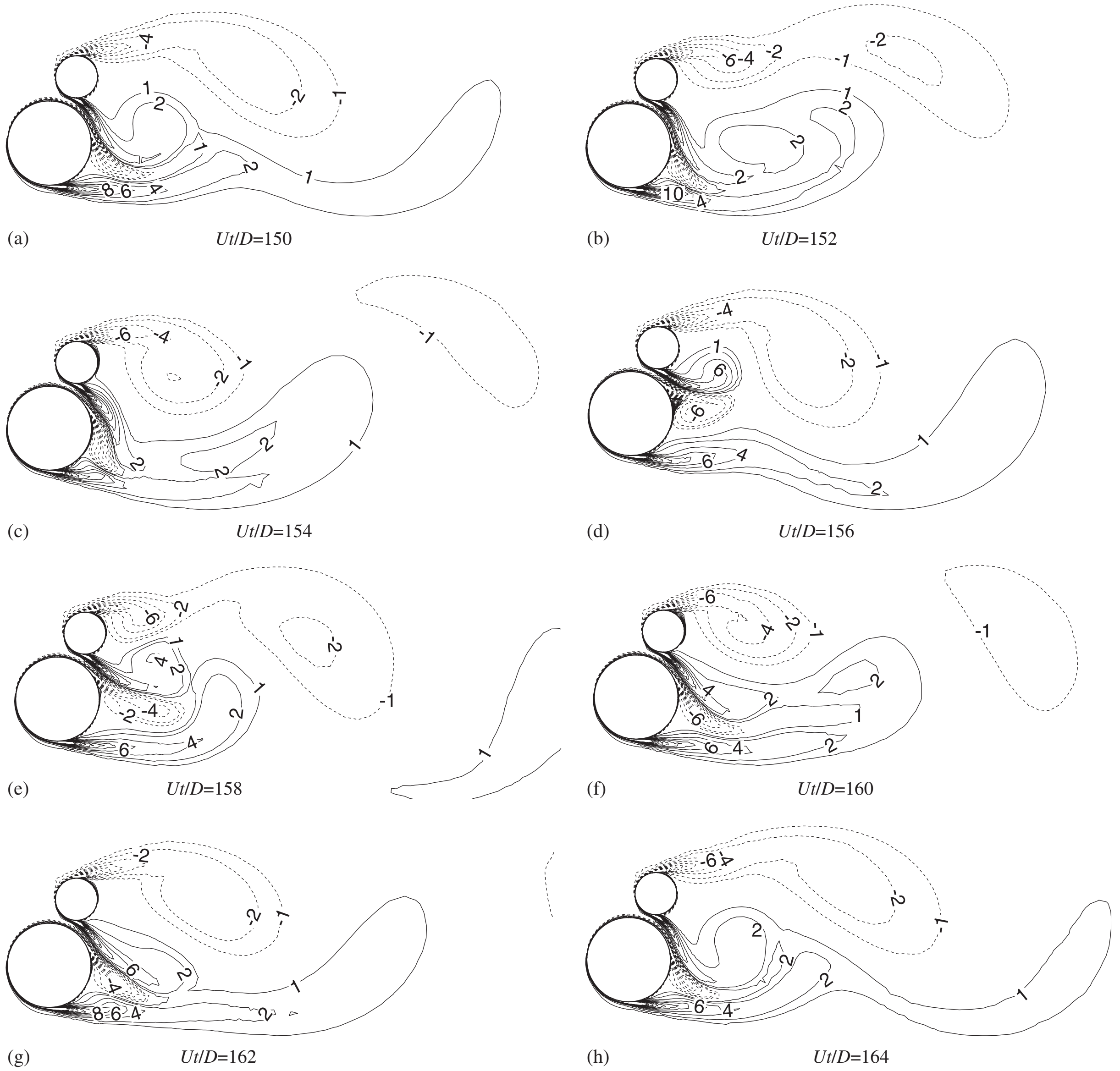

(a) Ut/D=150 (b) Ut/D=152

(c) Ut/D=154 (d) Ut/D=156

(e) Ut/D=158 (f) Ut/D=160

(g) Ut/D=162 (h) Ut/D=164

Fig. 22. Instantaneous vorticity contours behind the two cylinders for $G/D = 0.1$ and $\alpha = 112.5°$ (large cylinder $\mathrm{Re} = 5 \times 10^4$).

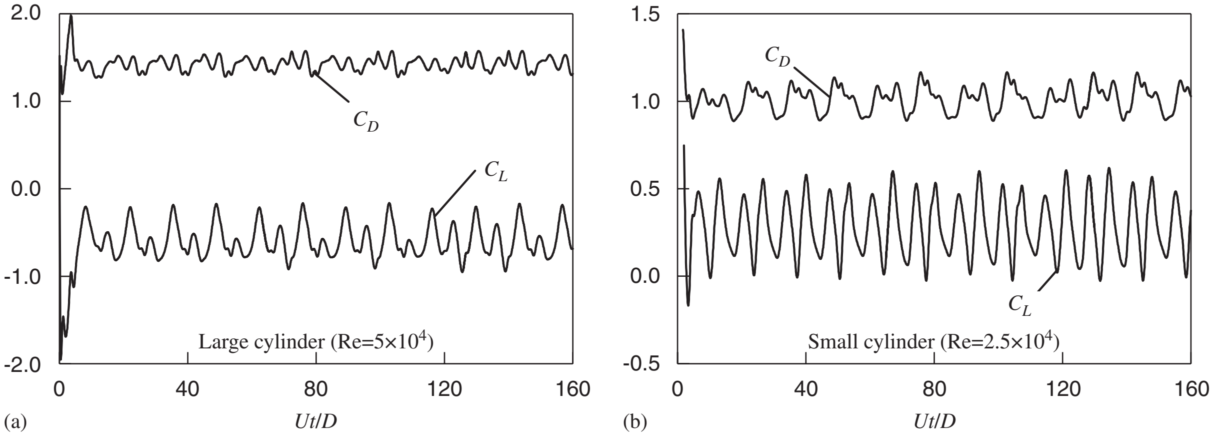

Fig. 23. Time history of the force coefficients on the two cylinders for $G/D = 0.1$ and $\alpha = 112.5°$.

means that the vortex shedding is in the interaction-shedding mode. It is interesting to see that the fluctuating lift contains the frequency components that are much higher than that on an isolated single cylinder for $G/D = 0.2$ and 0.4 and α between 90° and 135°.

4.3. *Effect of the diameter ratio d/D*

The effects of the diameter ratio d/D on the flow pattern and the forces on the cylinders are studied next. A constant position angle α of 90° is employed in examining the effect of d/D. The computations are carried out for $G/D = 0.05$, 0.1 and 0.2 and d/D ranging from 0.1 to 1.0 with an interval of 0.1. The Reynolds number based on the large cylinder diameter is 5×10^4. The mesh qualities in this section are similar to those of the previous section. The computational time step for all of the cases is set to be 0.002.

4.3.1. *Force coefficients on the cylinders*

Fig. 25 shows the variation of the time-averaged drag and lift coefficients on the large cylinder with the diameter ratio d/D for $G/D = 0.05$, 0.1 and 0.2. The mean drag coefficients on the large cylinder are always larger than that on an isolated cylinder for $\alpha = 90°$. It is seen from Fig. 25 that the mean drag on the large cylinder increases with the increase of d/D and the increase rate decreases with increasing G/D. For $G/D = 0.2$ the mean drag on the large cylinder almost does not change with the increase of d/D. The mean lift on the large cylinder is negative and its magnitude increases with the increase of d/D. The absolute value of the lift on the large cylinder increases when G/D decreases. Fig. 26 shows the variation of the time-averaged force coefficients on the small cylinder with d/D. With the increase of d/D, the mean drag on the small cylinder decreases for small value of d/D and increases for large value of d/D. The mean lift on the small cylinder is positive and its magnitude increases with the increase of d/D. By comparing Fig. 25(b) with Fig. 26(b), it can be seen that the mean lift on the large cylinder and that on the small cylinder is repulsive at all cases of G/D and d/D studied.

Fig. 27 shows the variation of the mean total force coefficients ($\bar{C}_{DE}$ and $\bar{C}_{LE}$) on the two-cylinder system with d/D which are defined using the equivalent diameter. The total drag coefficients in Fig. 27(a) are normalized by the mean drag coefficient ($\bar{C}_{D0}$) on an isolated cylinder at $\mathrm{Re} = 5 \times 10^4$. For $G/D = 0.05$ and 0.1, the mean total drag coefficient is larger than that on an isolated cylinder, and it increases with the increase of d/D. For $G/D = 0.2$, the mean total drag coefficient is larger than that on an isolated cylinder for $d/D > 0.6$ but is almost identical to that on an isolated cylinder for $d/D < 0.6$. It is seen from Fig. 27(a) that the mean total drag attains its maximum value when the two cylinders are of an identical diameter. The mean total lift coefficient is towards the large cylinder side ($\bar{C}_L < 0$) for small values of d/D. It increases with the increase of d/D and approaches zero when $d/D = 1.0$. By comparing Figs. 25(b), 26(b) and 27(b), it can be seen that the magnitude of the mean total lift coefficient is much smaller than that either on the large cylinder or that on the small cylinder, especially for large value of d/D. This is mainly because the lift coefficients on the two cylinders are repulsive.

Figs. 28 and 29 show the r.m.s. force coefficients on the large cylinder and those on the small cylinder, respectively. The r.m.s. drag coefficient on the large cylinder approaches to that on an isolated cylinder, when d/D is very small. It

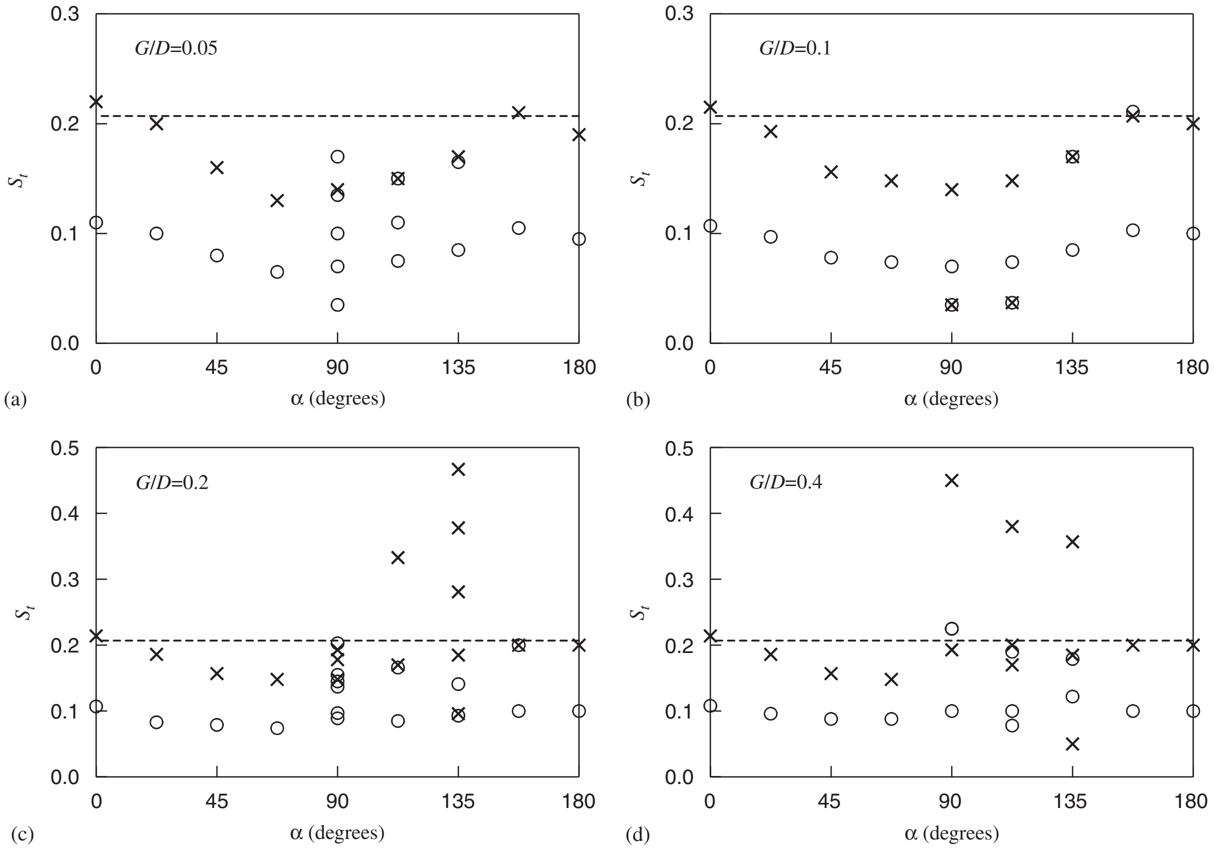

Fig. 24. Variation of the Strouhal number with α for different value of G/D (large cylinder $\mathrm{Re} = 5\times10^4$): ×, large cylinder; ○, small cylinder; - - - - -, isolated cylinder.

increases with the increase of d/D for the range of G/D investigated. The r.m.s. drag coefficient on the small cylinder decreases for small values of d/D and increases for large values of d/D with increasing d/D. The r.m.s. lift on the large cylinder attains its maximum value when $d/D = 0.1$, whereas that on the small cylinder is a maximum when $d/D = 1.0$. It can also be seen from Figs. 28(b) and 29(b) that the r.m.s. lift coefficient on the small cylinder is much smaller than that on the large cylinder when $d/D<0.5$. Fig. 30 shows the r.m.s. total drag coefficient (C'_{DE}) and r.m.s. total lift coefficient (C'_{LE}) based on the equivalent diameter on the two-cylinder system. The r.m.s. drag and the r.m.s. lift coefficients are normalized by their counterparts on an isolated cylinder $\left(C'_{D0}\text{ and }C'_{L0}\right)$, respectively. It is seen from Fig. 30(a) that the variations of the r.m.s. total drag coefficient with d/D may be different for different G/D. The r.m.s. total drag increases with increasing d/D for $G/D = 0.05$. For $G/D = 0.1$ and 0.2, the r.m.s. total drag decreases with increasing d/D for small values of d/D and increases for large values of d/D. The r.m.s. total drag increases with increasing G/D for d/D between 0.1 and 0.3 and decreases for d/D between 0.6 and 1.0. The r.m.s. total lift coefficient is always smaller than that on an isolated cylinder, regardless of d/D and G/D. It attains its maximum value when $d/D = 0.1$ in the computed three cases of G/D.

4.3.2. Vortex shedding frequency

The power spectra of the lift coefficient on the large cylinder and those on the small cylinder for $G/D = 0.2$ and $\alpha = 90°$ are plotted in Figs. 31 and 32, respectively. It can be seen that for small value of $d/D = 0.1$, the lift on two cylinders oscillates at a single frequency. The Strouhal number of the lift of the small cylinder in Fig. 32(a) is 0.1 times of that of the large cylinder in Fig. 31(a). For the medium value of $d/D = 0.3$, the fluctuating lift on the large cylinder has a single sharp peak, whereas the spectra of the lift on the small cylinder has multiple sharp peaks. The fluctuating lift on the small cylinder contains components that are of higher frequencies than those on an isolated cylinder. For the large

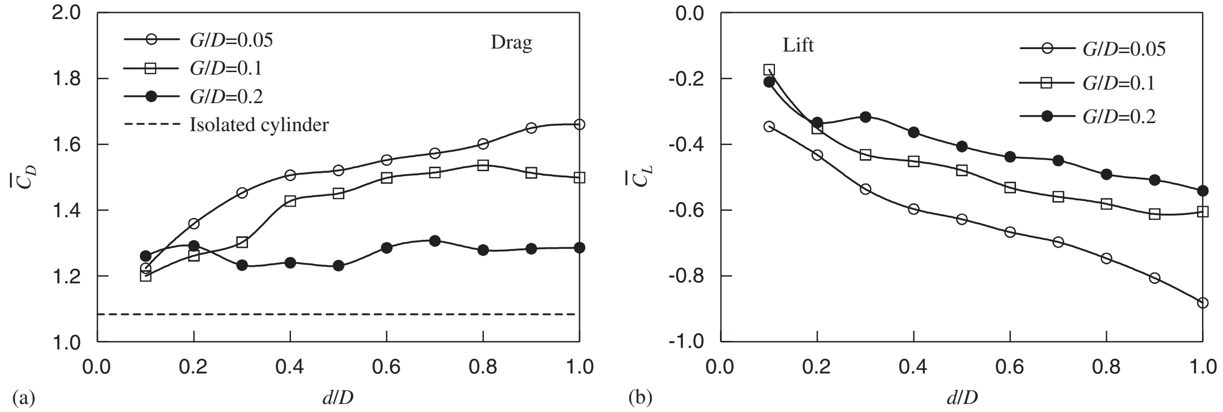

Fig. 25. Variation of the mean force coefficients on large cylinder with d/D (Re $= 5 \times 10^4$).

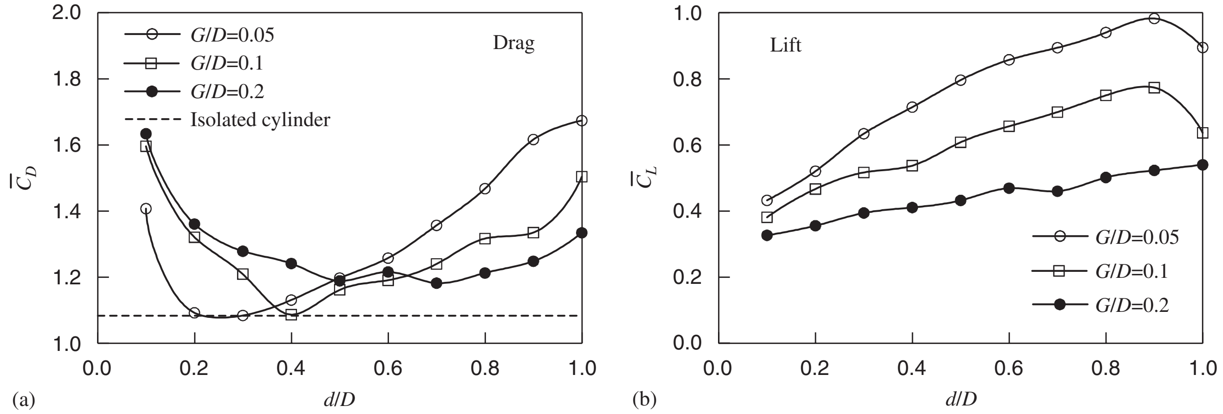

Fig. 26. Variation of the mean force coefficients on small cylinder with d/D (Re $= 2.5 \times 10^4$).

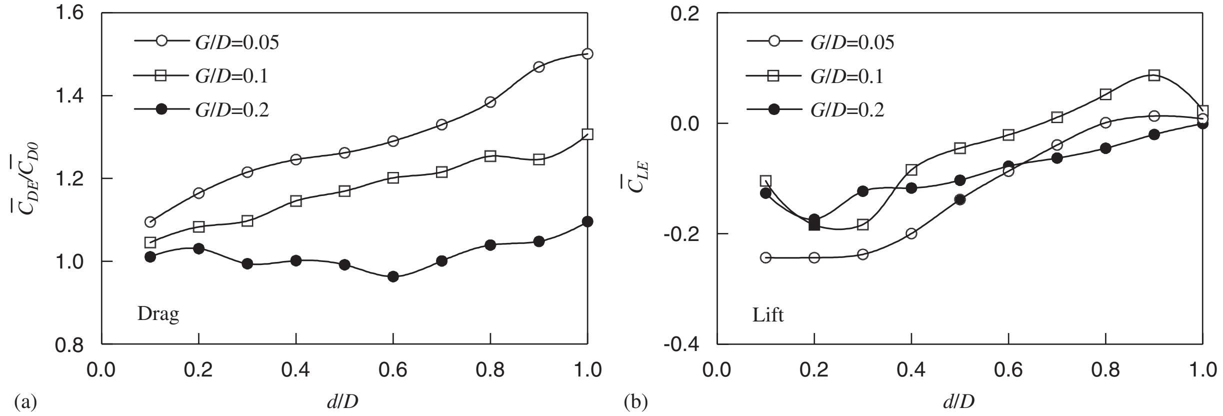

Fig. 27. Variation of the time-averaged total force coefficients with d/D (large cylinder Re $= 5 \times 10^4$).

value of $d/D = 0.9$, the lifts on both the large and small cylinders oscillate with multiple frequencies. It is observed that the flow patterns for small values of d/D are in the one-wake mode, whereas the flow patterns for medium and larger values of d/D are in the interaction-shedding mode as discussed in Section 4.2.3.

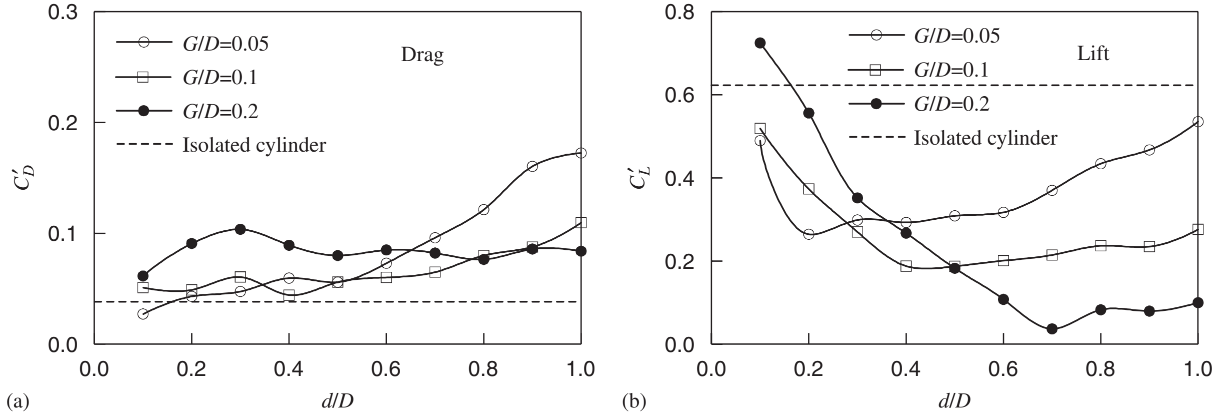

Fig. 28. Variation of the r.m.s. force coefficients on the large cylinder with d/D ($\mathrm{Re} = 5 \times 10^4$).

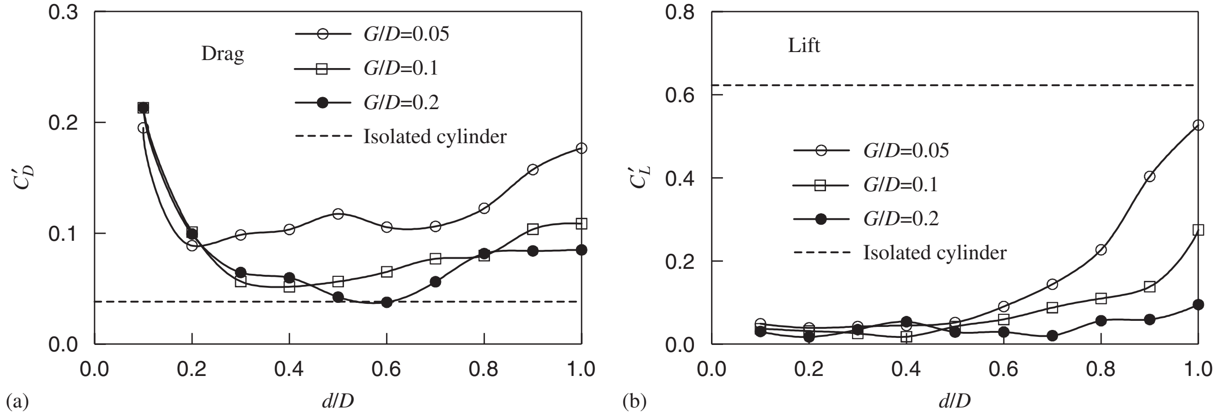

Fig. 29. Variation of the r.m.s. force coefficients on the small cylinder with d/D ($\mathrm{Re} = 2.5 \times 10^4$).

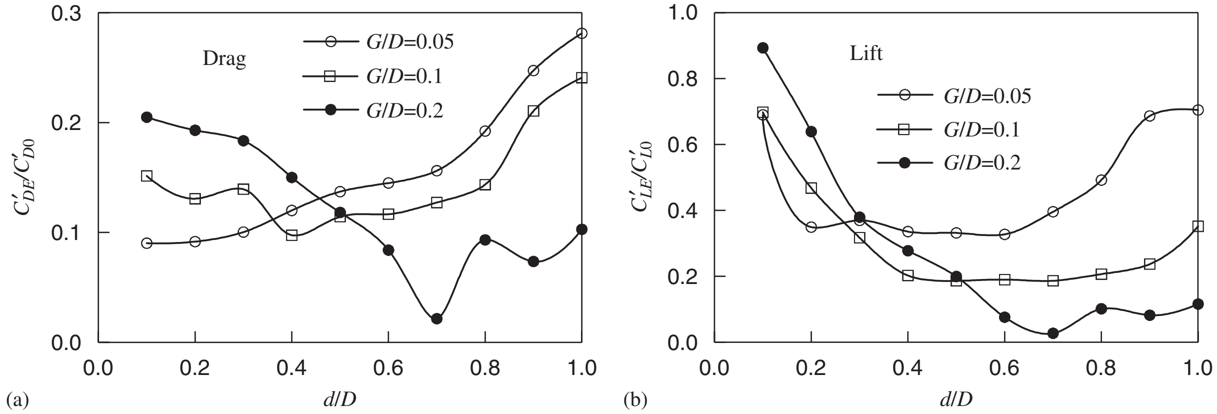

Fig. 30. Variation of the r.m.s. total force coefficients with d/D (large cylinder $\mathrm{Re} = 5 \times 10^4$).

Fig. 33 shows the variation of the Strouhal number of the fluctuation lift coefficient as a function of the diameter ratio for two gap ratios and $\alpha = 90^\circ$. It is seen that the lift coefficients of both cylinders oscillate with a single frequency for small values of d/D ($d/D \leqslant 0.3$ in Fig. 33(a) and (d)/$D \leqslant 0.1$ in Fig. 33(b)), and the Strouhal number of the small cylinder is d/D times that of the large cylinder. From Fig. 30(a) it can be seen that, when the d/D becomes large, the lift

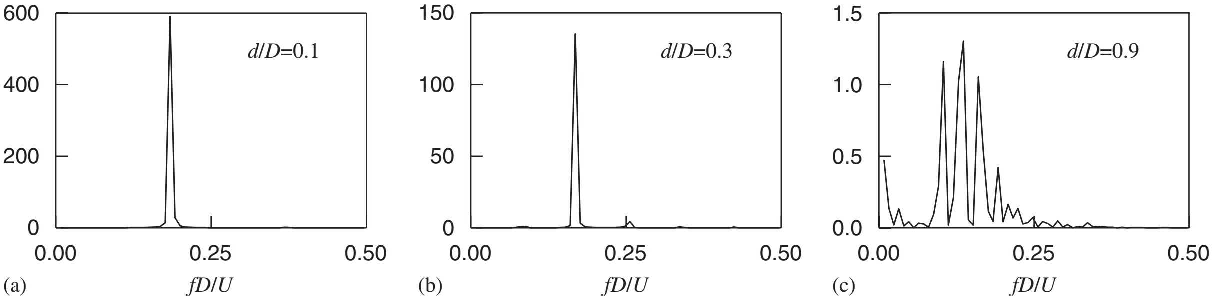

Fig. 31. Power spectra of the lift coefficient on the large cylinder for $G/D = 0.2$ and $\alpha = 90°$ ($\mathrm{Re} = 5 \times 10^4$).

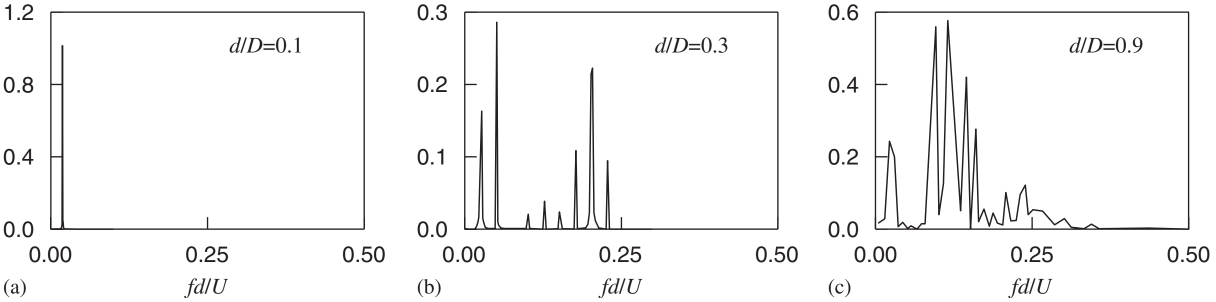

Fig. 32. Power spectra of the lift coefficient on the small cylinder for $G/D = 0.2$ and $\alpha = 90°$ ($\mathrm{Re} = 2.5 \times 10^4$).

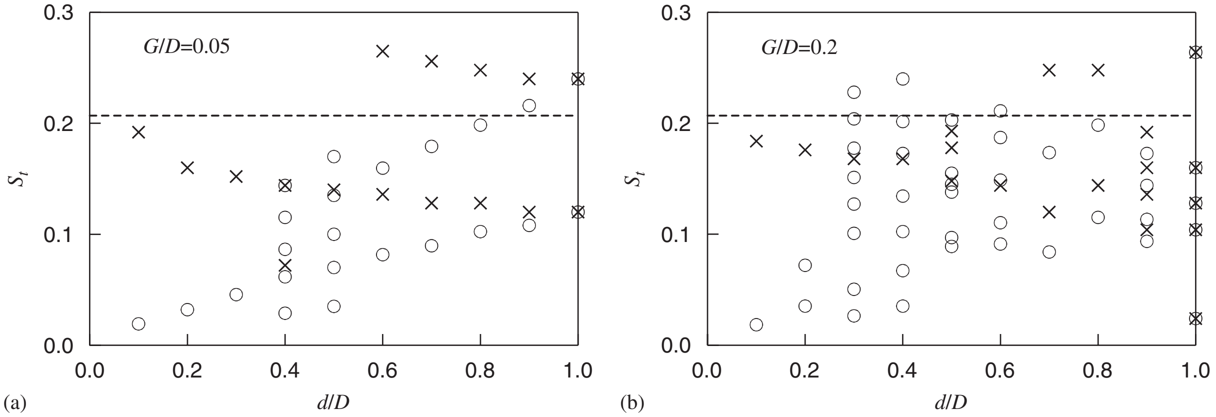

Fig. 33. Variation of Strouhal number with d/D for $\alpha = 90°$: ×, large cylinder ($\mathrm{Re} = 5 \times 10^4$); ○, small cylinder ($\mathrm{Re} = 2.5 \times 10^4$); - - - - -, isolated cylinder ($\mathrm{Re} = 5 \times 10^4$).

on the large cylinder has two nondimensional frequencies for most values of d/D, with one being smaller and the other larger than the Strouhal number of a single isolated cylinder. At the gap ratio $G/D = 0.2$, the lift on the large cylinder and that on the small cylinder fluctuate at several frequencies for larger values of d/D.

5. Conclusions

Vortex shedding flow past two circular cylinders of different diameters is studied numerically. The computations are carried out in the sub-critical Reynolds number regime. The numerical model is first verified by the experimental data.

Then the model is applied to study the effects of the small cylinder on the flow pattern and the force coefficients on the cylinders. The flow is calculated for a broad range of gap and diameter ratios. The major results can be summarized as follows.

1. Vortex shedding behind the cylinders can be classified into two modes. One is the one-wake mode in which the two cylinders behave as a single body. In the one-wake mode, the gap between the two cylinders has little effect on the shedding process and there is only one wake behind the cylinders. This mode is found when the two cylinders are in a near tandem arrangement or the small cylinder is located in the front upper side of the large cylinder. The other mode is the interaction-shedding mode, in which the shedding behind the cylinders is strongly affected by the shear layers behind the gap. This mode is found when the small cylinder is located in the rear upper side of the large cylinder for the cases of gap ratios studied. It is found that the range of the angle α in which the interaction-shedding mode occurs expands as the gap ratio G/D increases.
2. The lift on the large cylinder and that on the small cylinder oscillate at a single dimensional frequency when the flow is in the one-wake mode. When the flow is in the interaction-shedding mode, the spectra of the lift on the cylinders have two or more sharp frequency peaks.
3. The time-averaged mean drag on the large cylinder attains the maximum value when α is around 90° and the mean drag on the small cylinder attains its maximum value when α is around 60°. The drag on both cylinders is smaller than that on an isolated cylinder when the two cylinders are in near tandem arrangement. A negative drag on the small cylinder is also observed when the small cylinder is directly behind the large cylinder. The maximum mean lift on the large cylinder occurs at α about 120° and is negative. The maximum mean lift on the small cylinder occurs at α about 45° and is positive. The variation of the mean total drag coefficient on the two-cylinder system (based on the equivalent diameter) with α is very similar to that of the mean drag on the large cylinder. It is about 0.5 times that on an isolated cylinder when $\alpha = 0^\circ$ and 180°. It increases when the small cylinder moves from the rear or the front to the side of the large cylinder and attains its maximum value when α is around 90°. The variation of the mean total lift is different from either that of the large cylinder or that of the small cylinder. It approaches zero at $\alpha = 0^\circ$, 90° and 180°, and attains its maximum value when α is around 67.5° and 157.5°.
4. The r.m.s. drag coefficients on both the large cylinder and that on the small cylinders are smaller than that on an isolated cylinder when the two cylinders are in near tandem arrangement. The r.m.s. total drag coefficient on the two-cylinder system is larger than that on an isolated cylinder when α is around 90° and smaller when α is around 0° or 180°. The r.m.s. lift coefficients of the large and the small cylinder and the r.m.s. total lift coefficients are smaller than that on an isolated cylinder.
5. The effect of the diameter ratio is investigated for cases of $\alpha = 90^\circ$. The mean drag on the large cylinder increases and the mean lift on the large cylinder decreases with increasing d/D. The mean drag coefficient on the large cylinder, the small cylinder and the two-cylinder system is larger than that on an isolated cylinder. The mean total lift on the two-cylinder system is much smaller than that on either the large or the small cylinder, especially at large values of d/D. The r.m.s. drag on the large cylinder increases and the r.m.s. lift on the large cylinder decreases with increasing d/D. The r.m.s. total drag coefficients may be larger or smaller than that on an isolated cylinder, depending on d/D and G/D. The r.m.s. total lift coefficient is always smaller than that on an isolated cylinder. It is found that the flow is in the one-wake mode for small values of d/D and in the interaction-shedding mode for large values of d/D.

Acknowledgements

The authors would like to acknowledge the support from Australia Research Council through ARC Discovery Projects Program Grant No. DP0557060 and the National Natural Science Foundation of China under the Grant 50428908.

References

Bearman, P.W., Wadcock, A.J., 1973. The interaction between a pair of circular cylinder normal to a stream. Journal of Fluid Mechanics 61, 499–511.

Brooks, A.N., Hughes, T.J.R., 1982. Streamline upwind/Petrov–Galerkin formulations for convection dominated flows with particular emphasis on the incompressible Navier–Stokes equations. Computer Methods in Applied Mechanics and Engineering 32, 199–259.

Brørs, B., 1999. Numerical modeling of flow and scour at pipelines. Journal of Hydraulic Engineering 125, 511–522.

Dalton, C., Xu, Y., Owen, J.C., 2001. The Suppression of lift on a circular cylinder due to vortex shedding at moderate Reynolds numbers. Journal of Fluids and Structures 15, 617–628.

Guilmineau, E., Queutey, P., 2004. Numerical simulation of vortex-induced vibration of a circular cylinder with low mass-damping in a turbulent flow. Journal of Fluids and Structures 19 (4), 449–466.

Jester, W., Kallinderis, Y., 2003. Numerical study of incompressible flow about fixed cylinder pairs. Journal of Fluids and Structures 17, 561–577.

Kelly, D.W., Nakazawa, S., Heinrich, J.C., 1980. A note of upwinding and anisotropic balancing dissipation in finite element approximations to convective diffusion problems. International Journal of Numerical Methods in Engineering 15, 1705–1711.

Lam, K., Li, J.Y., So, R.M.C., 2003. Force coefficients and Strouhal numbers of four cylinders in cross flow. Journal of Fluids and Structures 18, 305–324.

Liang, D., Cheng, L., 2005. Numerical modeling of flow and scour below a pipeline in currents Part I. Flow simulation. Coastal Engineering 52, 25–42.

Meling, T.S., Dalherim, J., 1997. Numerical prediction of the response of a vortex-excited cylinder at low Reynolds number. Proceedings Seventh International Offshore and Polar Engineering Conference, Honolulu, vol. 3, pp. 25–30.

Meneghini, J.R., Saltara, F., Siqueira, C.L.R., Ferrari Jr., J.A., 2001. Numerical simulation of flow interference between two circular cylinders in tandem and side-by-side arrangements. Journal of Fluids and Structures 15, 327–350.

Menter, F.R., 1993. Zonal two-equation k–ω turbulence models for aerodynamics flows. AIAA 24th Fluid Dynamics Conference, Orlando, FL, USA.

Sakamoto, H., Haniu, H., 1994. Optimum suppression of fluid forces acting on a circular cylinder. ASME Journal of Fluids Engineering 116, 221–227.

Sakamoto, H., Tan, K., Haniu, H., 1991. An optimum suppression of fluid forces by controlling a shear layer separated from a square prism. ASME Journal of Fluids Engineering 113, 183–189.

Schewe, G., 1983. On the force fluctuations acting on a circular cylinder in cross flow from subcritical up to transcritical Reynolds numbers. Journal of Fluid Mechanics 133, 265–285.

Selvam, R.P., 1997. Finite element modeling of flow around a circular cylinder using LES. Journal of Wind Engineering and Industrial Aerodynamics 67&68, 129–139.

So, R.M.C., Savkar, S.D., 1981. Buffeting forces on rigid circular cylinders in cross flows. Journal of Fluid Mechanics 105, 397–425.

Strykowski, B.J., Sreenivasan, K.R., 1990. On the formation and suppression of vortex 'shedding' at low Reynolds numbers. Journal of Fluid Mechanics 218, 71–107.

Tadrist, H., Martin, R., Tadrist, L., 1990. Experimental investigation of fluctuating forces exerted on a cylindrical tube (Reynolds numbers from 3000 to 30,000). Physics of Fluids A 2 (12), 2176–2182.

Tsutsui, T., Igarashi, T., Kamemoto, K., 1997. Interactive flow around two circular cylinders of different diameters at close proximity. Experiment and numerical analysis by vortex method. Journal of Wind Engineering and Industrial Aerodynamics 69–71, 279–291.

Wilcox, D.C., 1988. Reassessment of the scale-determining equation for advanced turbulence models. AIAA Journal 26 (11), 1299–1310.

Wilcox, D.C., 1994. Simulation of transition with a two-equation turbulence model. AIAA Journal 32 (2), 247–255.

Williamson, C.H.K., 1985. Evolution of a single wake behind a pair of bluff bodies. Journal of Fluid Mechanics 159, 1–18.

Zdravkovich, M.M., 1977. Review of flow interference between two circular cylinders in various arrangements. ASME Journal of Fluids Engineering 99, 618–633.

Zdravkovich, M.M., 1987. The effects of interference between circular cylinders in cross flow. Journal of Fluids and Structures 1, 239–261.

Zhao, M., Cheng, L., Teng, B., Liang, D., 2005. Numerical simulation of viscous flow past two circular cylinders of different diameters. Applied Ocean Research 27, 39–55.